Mechatronics 81 (2022) 102696

Contents lists available at ScienceDirect

Mechatronics

journal homepage: www.elsevier.com/locate/mechatronics

High energy efficiency oriented-control and design of WFSM based on driving condition of electric vehicle

Min-Ro Park [a], Dong-Min Kim [b], Young-Hoon Jung [c], Myung-Seop Lim [d,*]

[a] Interactive Robotics R&D Division, Korea Institute of Robotics & Technology Convergence, Pohang 37553, South Korea
[b] Department of Automotive Engineering, Honam University, Gwangju 62399, South Korea
[c] R&D Division, Hyundai Motor Company, Hwaseong 18280, South Korea
[d] Department of Automotive Engineering, Hanyang University, Seoul 04763, South Korea

ARTICLE INFO

Keywords:
Driving cycle
Electric vehicle
Energy efficiency
Traction motors
Wound-field synchronous motor.

ABSTRACT

The purpose of this paper is to increase the energy efficiency of an electric vehicle (EV) with a wound-field synchronous motor (WFSM). Therefore, methods are proposed to estimate and improve the energy efficiency of the EV as well as the performance of the WFSM. The following contributions are provided: 1) EV model as well as the mathematical model of the electric motor are explained considering the common Artemis driving cycle (CADC); 2) a control method for maximizing the energy efficiency of the electric motor is proposed; 3) analysis methods for calculating the circuit parameters (resistance, inductance, and flux linkage) and losses (ohmic, iron, and mechanical loss) are described. The efficiency of the machine is accurately determined using the proposed analysis method; 4) based on the proposed methods, the design process of the WFSM is proposed to improve the energy efficiency considering the vehicle system and driving cycle; and 5) the proposed methods are verified through tests of the prototype and improved motor. As a result, through the proposed design and control method, even though the volume of the improved motor was 7.8% smaller than that of the prototype, the efficiency of the improved motor was higher than that of the prototype in all regions. In addition, to confirm the effectiveness of the proposed methods, the performance of the electric vehicle considering the driving cycle was analyzed according to the characteristics of the electric motor. The energy loss of the improved motor with the proposed control and design method was 63.3% less than that of the prototype. Accordingly, the energy efficiency of the vehicle system and the energy consumption of the battery increased by 7.8%p and decreased by 2.0 kWh, respectively.

1. Introduction

Recently, as the demand for electric vehicles (EVs) has increased, various characteristics of the electric motors used for EV traction have been extensively studied. To achieve a high efficiency and power density, permanent magnet synchronous motors (PMSMs) employing rare-earth permanent magnets (PMs) have been used as traction motors for EVs [1–4]. Therefore, the design methods for PMSMs have been extensively studied [5–10]. However, rare-earth PMs are highly costly and are associated with unstable supply [11]. These issues have led to numerous studies on motors without rare-earth elements such as neodymium (Nd) and dysprosium (Dy) [12–15]. Therefore, the induction motors have been extensively studied as rare-earth free motor; however, their efficiency and power density need to be increased [16, 17]. Additionally, PMSMs that operate at high speeds under a constant magnetic flux of the PM require high voltages. This requirement burdens the inverter and vehicle system. Therefore, the variable-flux (VF) PMSM, which can control the magnetic flux of the PM is widely studied. The magnetic flux of the PM is controlled by changing the magnetization state (MS) through the stator current. Therefore, to accurately predict the MS of the PM, an accurate material property of the PM is needed [18]. Furthermore, an additional current and its control algorithm are required to change the MS according to the various operating points of the electric motor. Also, many studies have been performed to improve the torque density of the VF-PMSM using PMs of various types and sizes [19, 20].

These problems can be solved using a wound-field synchronous

This paper was recommended for publication by Associate Editor Roger Dixon Role
* Corresponding author.
E-mail address: myungseop@hanyang.ac.kr (M.-S. Lim).

https://doi.org/10.1016/j.mechatronics.2021.102696
Received 31 December 2020; Received in revised form 21 June 2021; Accepted 29 October 2021
Available online 25 November 2021

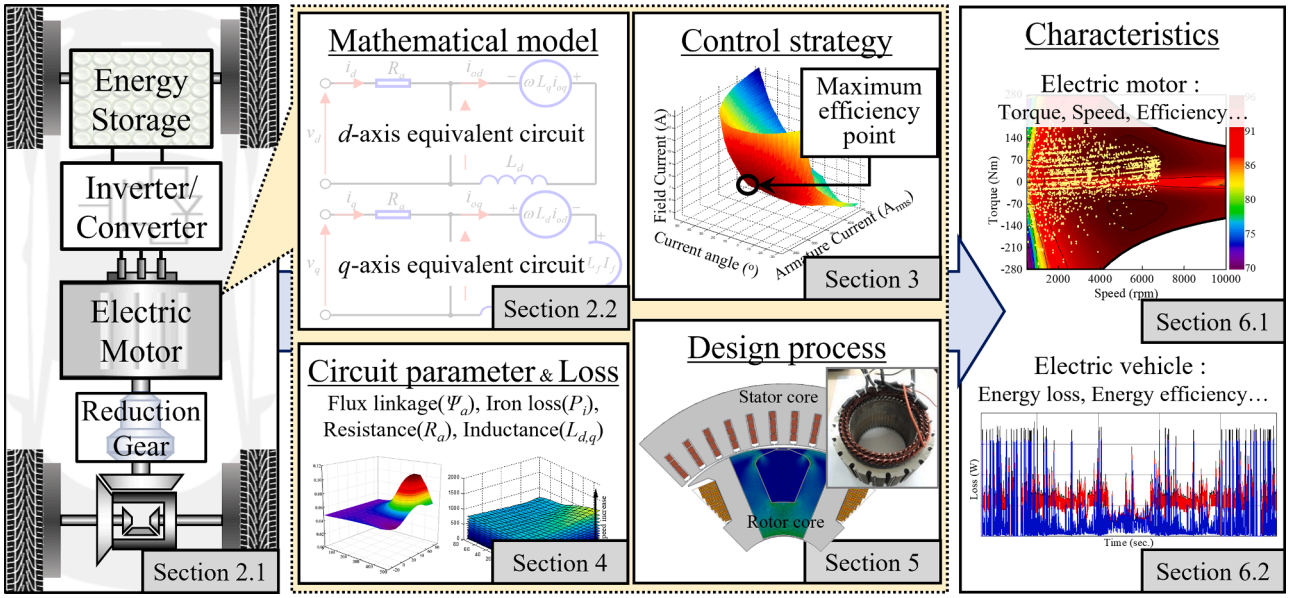

Fig. 1. Process of analysis for EV with electric motor.

motor (WFSM) [21–24]. The WFSM without PMs is advantageous for operations at high speeds. This is because, in contrast to the PMSM, the field flux can be adjusted by directly controlling the field current in the WFSM. Therefore, the WFSM has extra degrees of freedom in both the design and control, compared with other motor types. Moreover, because both the magnetic and reluctance torques are used through the vector control of the armature current, the WFSM has a higher torque than other types of rare-earth free motors. Therefore, it is widely used not only for EV traction, but also for various vehicle applications. Nevertheless, the efficiency of the WFSM is lower than that of the PMSM owing to the additional losses incurred on the field coil and the brush of the rotor.

[25–28] described a brushless WFSM without the brush and slip ring, which are disadvantages of the conventional WFSM. However, these papers only propose structural concepts based on simulation rather than analysis on characteristics such as efficiency and torque. Also, design and control methods improving the performance of the WFSM have been studied. In [29–34], a design method for improving the torque characteristics of the WFSM was proposed. However, these studies did not suggest methods for enhancing efficiency. [35] increased the efficiency by placing PMs as consequent pole in the existing WFSM. However, this method weakens the advantages of WFSM which does not use PMs, such as [29–31]. In [36] and [37], the iron loss significantly affected the performance of the WFSM. Nevertheless, [23] presented a control scheme minimizing the copper loss of the WFSM. This scheme does not maximize the efficiency, as it considers only the copper loss. In addition, in [34, 38], the WFSM is still controlled by the maximum torque per ampere (MTPA) control method. This method is not a solution for increasing the efficiency of the motor as well as enhancing the energy efficiency of electric vehicle systems. [39, 40] show sensorless control that estimates the position of the rotor without a sensor. [41, 42] present a method to effectively control the field current. However, these studies do not include an analysis of the efficiency of WFSM. [43] improved the efficiency and performance of WFSM in terms of control. A control that effectively utilizes the extra control degree of freedom in the WFSM is presented. In [24], a method for improving the efficiency of the WFSM was proposed. However, this method requires additional switching hardware, space, and a control method. [44] describes how to increase the efficiency of WFSM. However, the electromagnetic characteristics (skin, proximity effect and cross saturation effect) and mechanical characteristics (structural stability of the rotor) were not considered. In addition, drivetrain parts other than the electric motor were ignored, and the characteristics of the electric motor were not reflected during regenerative braking. [45] addressed the efficiency improvement of the WFSM, but the results were not experimentally validated.

This paper proposes estimation and improvement methods for the energy efficiency of the EV using the WFSM. Through the methods proposed in this paper, the characteristics of the electric motor are accurately calculated according to the design and control method of the electric motor, and it is possible to quantitatively confirm how much they affect the vehicle system. The proposed methods are shown in Fig. 1 and its contents are as follows:

1 EV model for system simulation (Section 2).

1) Modeling of the EV including the inverter, converter, energy storage, and electric motor based on the data and reference of each component.
2) Calculation of operating points for the electric motor based on the EV model.

2 Control strategy of the WFSM to maximize energy efficiency (Section 3).

1) Analysis of the characteristics of the electric motor and vehicle when applying commonly used MTPA control to the WFSM.
2) The proposal of a control method to improve the efficiency of the WFSM.
3) An efficient algorithm for the WFSM using an analytic method.

3 Parameters and loss analysis method to calculate motor characteristics accurately (Section 4).

1) Accurate and detailed methods for the analysis of the circuit parameters and losses in the electric motor using analytic, numeric, and experimental methods.

4 Design process of the electric motor considering system characteristics (Section 5).

1) Design direction to improve energy efficiency based on the driving cycle.

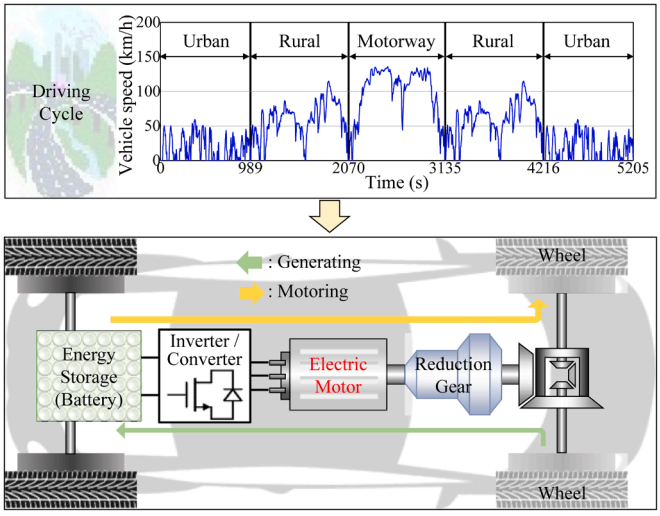

Fig. 2. Electric vehicle system.

Table 1
Specification of EV System.

Items		Value	Unit
Driving Condition [50–56]	Air density	1.2	kg/m^3
	Air drag coefficient	0.29	–
	Rolling resistance coefficient	0.01	–
	Driving cycle	CADC	–
Target Vehicle [57]	Glider weight	1100	kg
	Width	1.80	m
	Height	1.57	m
	Wheelbase	2.6	m
	Wheel radius (tire included)	0.334	m
	Accessory	600	W
Reduction Gear [58]	Gear ratio	6.54:1	–
	Maximum efficiency	92	%
	Weight	28	kg
Energy Storage [59, 60]	Type	LiFePO4	–
	Nominal voltage	358	V
	Nominal current	170	A
	Nominal capacity	61	kWh
	Series connection	102	–
	Parallel connection	68	–
	Weight	485.5	kg
Converter [61, 62]	Output power	140.35	kW
	Output DC voltage	360	V
	Output direct current	390	A
	Efficiency	98	%
	Weight	2.09	kg
Inverter [61, 62]	Output power	133.33	kW
	Output line to line voltage	207.85	V_{rms}
	Output line current	450	A_{rms}
	Efficiency	95	%
	Weight	11.11	kg
Electric Motor	Output power	120	kW
	Weight	<45	kg

2) Geometric design considering the efficiency and power density.

- Rectangular conductor and a hairpin coil to reduce the losses [46–49].
- Core shape of rotor and stator using analytical methods.
- Number of turns of the armature winding and the axial length considering the power density.

Finally, in Section 6, the characteristics of the designed electric motor, such as the torque and efficiency, are evaluated via the analysis methods of the circuit parameters and losses proposed in Section 4. Also, the prototype and improved motors are applied to the vehicle system to calculate the characteristics of the EV considering the driving cycle. Lastly, the proposed methods are verified through tests of the prototype and improved motor.

2. EV model considering electric motor

2.1. EV model

The investigated EV is a mid-sized vehicle that can be operated in various environments, including urban, rural, and motorway. The drivetrain uses one electric motor connected to the front axle via the differential and reduction gear. The reduction gear ratio affects the operating range of the vehicle. To satisfy the operating range of the vehicle, a higher reduction gear ratio makes the electric motor operate at a higher speed. Furthermore, a high reduction gear ratio can reduce the torque demand, resulting in a compact size of the electric motor. However, if the reduction gear ratio is too high, so will be the operating speed of the electric motor. Consequently, the mechanical stability of the electric motor can be reduced. Therefore, an appropriate reduction gear ratio is needed. The required torque and speed of the electric motor under driving conditions are calculated using lateral vehicle dynamic equations. The vehicle dynamic equations consider the vehicle acceleration and resistive forces, and the latter include the rolling, grading, and air drag resistances [50].

The resistive force acting on the vehicle is an important parameter for calculating the vehicle behavior and determining the specification of the electric motor. There are three resistive forces acting on the vehicle: rolling resistance (F_r), grade resistance (F_g), and aerodynamic drag force (F_d). The description and equation of each resistance are as follows.

1) Rolling resistance force: When the tires roll on the surface, the force that resists motion.

$$F_r = f_r M_V g\cos\theta \tag{1}$$

2) Aerodynamic drag force: the force that resists the movement of a vehicle traveling at a specific speed in the air.

$$F_d = \frac{1}{2}\rho A_f C_d (V_V + V_w)^2 \tag{2}$$

3) Grade resistance force: When the vehicle moves up and down the slope, the force generated in the downward direction from the weight.

$$F_g = M_V g\sin\theta \tag{3}$$

where, f_r is the rolling resistance coefficient, M_V is the mass of the vehicle, θ is the longitudinal slope angle, g is the gravitational acceleration, ρ is the density of the air, A_f is the frontal area of the vehicle, C_d is the aerodynamic drag coefficient, V_V is the vehicle speed, and V_W is the wind speed.

The total resistive force ($F_{Resistive}$) is defined as the sum of the three resistive forces as follows:

$$F_{Resistive} = F_r + F_d + F_g \tag{4}$$

the tractive force (F_T) is calculated as (5) considering the resistive force, mass, and acceleration of the vehicle.

$$F_T = F_{Resistive} + M_V a \tag{5}$$

where, a is the acceleration of the vehicle.

The required torque (T_m) and rotational speed (n_m) of the electric motor are calculated through the tractive force, the vehicle speed, and

Table 2
Common Artemis Driving Cycle.

Items	Urban	Rural	Motorway	Unit
Travel Time	989	1081	1065	s
Travel Distance	4.87	17.27	28.74	km
Idle Time	278	32	13	s
Number of Stop	22	4	2	–
Maximum Speed	57.7	111.5	131.8	km/h
Average Speed	17.73	57.52	97.14	km/h
Maximum Deceleration	−3.14	−4.08	−3.36	m/s^2
Average Acceleration	0.73	0.49	0.41	m/s^2
Average Deceleration	−0.78	−0.52	−0.5	m/s^2

the gear ratio.

$$T_m = \frac{r_W F_T}{n_G} \tag{6}$$

$$n_m = \frac{60}{2\pi r_W} n_G V_V \tag{7}$$

where, r_W is the wheel radius, and n_G is the gear ratio.

Then, the required power (P_m) of the electric motor is calculated as (8) based on the required torque and rotational speed of the electric motor.

$$P_m = T_m n_m \frac{2\pi}{60} = F_T V_V \tag{8}$$

As shown in Fig. 2, the EV model includes the electric motor, energy storage, and mechanical parts. However, many studies ignore drivetrain parts excluding electric motor [6–9, 44]. To calculate the driving points of the electric motor and evaluate the characteristics of the vehicle system, each part of the drivetrain must be considered.

The specifications for each part of the EV model are presented in Table 1. First, the common Artemis driving cycle (CADC) is used as the reference driving cycle. The CADC reflects the actual operating conditions as a criterion for determining whether a new cycle is suitable and consists of low-speed urban, mid, high-speed rural, and high-speed motorway driving conditions representing various real situations [51–56]. Therefore, the CADC is adopted as the standard driving cycle used for calculating the performance of an EV, including an electric motor. The CADC is presented in Table 2 and Fig. 2. The target vehicle is a 'KONA electric' made by the Hyundai Motors [57]. The specification of the reduction gear is determined by referring to a 'eGearDrive series' from BorgWarner [58]. A lithium-ion battery is adopted as the resistance-capacitance equivalent circuit for energy storage [59, 60]. The chemistry for this battery is LiFePO4. The number of series connections is determined according to the nominal voltage and nominal current. The number of parallel connections is determined according to the capacity. The weight is obtained from the number of connected battery cells. The voltage and current specifications of the inverter are determined by considering the SVPWM and the characteristics of the switching device. In addition, the weights of the inverter and direct current (DC)/DC converter are derived using the power to weight ratio [61, 62]. The most important part of the EV, i.e., the electric motor, is described in Section 2.2. The electrical input limit of the electric motor is determined according to the specifications of the inverter and battery. Through this EV model, the driving points of the electric motor is calculated, and how the characteristics of the vehicle system change according to the design and control method of the electric motor is predicted.

The vehicle simulations considering the presented driving cycle and components are performed through advanced vehicle simulator (ADVISOR), a MATLAB/Simulink-based software [63].

2.2. Mathematical model of electric motor

In this paper, the characteristics of the electric motor are calculated using the voltage, current and torque equations based on the *d*- and q-axis equivalent circuits considering the iron loss [29, 64–66]. The voltage and current equations are expressed as (9)-(13).

$$V_a = \sqrt{v_d^2 + v_q^2} \tag{9}$$

$$I_a = \sqrt{i_d^2 + i_q^2} \tag{10}$$

$$\begin{bmatrix} v_d \\ v_q \end{bmatrix} = R_a \begin{bmatrix} i_d \\ i_q \end{bmatrix} + \begin{bmatrix} v_{od} \\ v_{oq} \end{bmatrix} \tag{11}$$

$$\begin{bmatrix} v_{od} \\ v_{oq} \end{bmatrix} = \begin{bmatrix} 0 & -\omega L_q \\ \omega L_d & 0 \end{bmatrix} \begin{bmatrix} i_{od} \\ i_{oq} \end{bmatrix} + \begin{bmatrix} 0 \\ \omega L_f I_f \end{bmatrix} \tag{12}$$

$$\begin{bmatrix} i_d \\ i_q \end{bmatrix} = \begin{bmatrix} -I_a \sin\beta \\ I_a \cos\beta \end{bmatrix} = \begin{bmatrix} i_{od} \\ i_{oq} \end{bmatrix} - \begin{bmatrix} i_{cd} \\ i_{cq} \end{bmatrix} \tag{13}$$

The shaft torque is calculated using (14), which considers the mechanical loss.

$$T_{shaft} = p\left[\left(L_f I_f i_{oq}\right) + \left(L_d - L_q\right) i_{od} i_{oq}\right] - \left(\frac{P_{mech}}{\omega_m}\right) \tag{14}$$

where V_a and I_a are the magnitude of voltage and current vector in the armature; the subscripts *d* and *q* refer to the *d*- and *q*-axis components. i_d and i_q are the input armature currents; v_d and v_q are the armature voltages; i_{od} and i_{oq} are the magnetizing currents; i_{cd} and i_{cq} are the iron loss currents; Ra is the phase resistance of the armature winding and R_c is the equivalent resistance of the iron loss; L_d and L_q are the inductances; L_f is the mutual inductance between the field and armature winding; I_f is the field current; p is the number of pole-pairs; ω and ω_m are the electrical and mechanical angular velocity, respectively; T_{shaft} is the shaft torque; P_{mech} is the mechanical loss; β is defined as the angle between the armature current vector and the *q*-axis.

As indicated by (9)-(14), there are many combinations of the magnitude and phase angle of the armature current and field currents that satisfy the target torque at any speed. Moreover, the electric motor performance depends on these current conditions. Thus, the current control method is a key factor affecting the performance of the electric motor. Therefore, the method for determining the current condition to maximize the efficiency is described in the next section.

3. Control strategy of WFSM

To maximize the energy efficiency of an EV, the electric motor must be controlled at the maximum efficiency. Therefore, the total loss (including field copper loss, iron loss, and armature copper loss) should be minimized. However, the generally used MTPA control method determines the armature current vector of the minimum magnitude that satisfies the target torque and input power limit [67, 68]. In particular, the WFSM is also controlled by the MTPA control method [34, 38]. Therefore, the maximum field current should be input to minimize the armature current. This solution minimizes only the armature copper loss and reduces the degree of freedom of field current control. In addition, the effect of iron loss on the efficiency of the WFSM is significant [36, 37]. Nevertheless, a control that minimize only copper loss are sometimes applied to WFSM [23]. Thus, a control method is required to minimize the total loss and take advantage of the degree of freedom. As mentioned previously, unlike the PMSM, because the WFSM has an additional variable (field current, I_f), an efficient process for maximum efficiency control is required considering the field current. For this reason, a maximum efficiency control with a simple process is proposed based on the *d, q*-axis voltage equation, and the torque equation, as

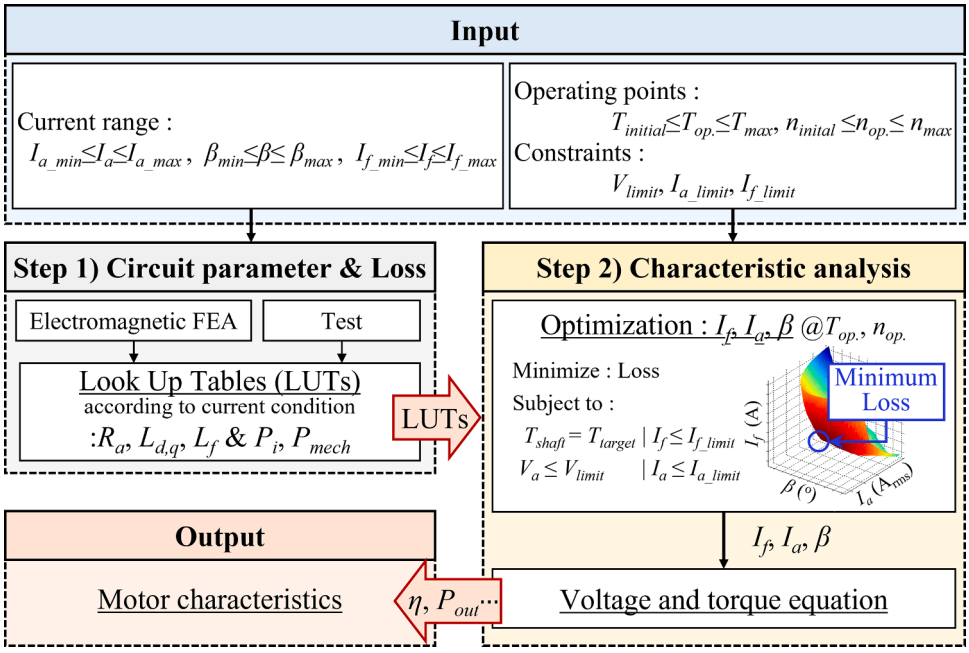

Fig. 3. Process of the maximum efficiency control.

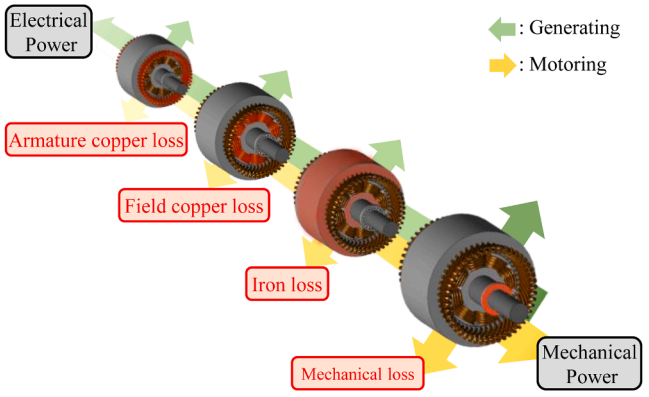

Fig. 4. Power flow of the WFSM.

expressed in (9)-(14). A control process for the maximum efficiency is shown in Fig. 3.

Step 1. Circuit parameter & loss

- Electromagnetic FEA: circuit parameters & iron loss are calculated and stored as loot up tables (LUTs).
- Test: LUTs of the mechanical loss is obtained from the no-load test.

Step 2. Characteristics analysis

- Optimization: current condition is determined to minimize the total loss based on the LUTs.
- Voltage and torque equations: using the current condition, the motor characteristics are evaluated.

Step 1 is a pre-process, where the LUTs to be used in Step 2 are stored. The LUTs of circuit parameters (i.e., armature resistance R_a, d, q-axis inductances $L_{d,q}$, field inductance L_f, and iron loss P_i according to current and frequency) and mechanical loss P_{mech} are estimated through the FEA and no-load test, respectively. The detailed calculation methods are presented in Section 4.

The main process, Step 2, involves searching for current conditions that satisfy maximum efficiency and evaluating motor characteristics that reflect this current condition. This step is repeated at each operating points of the electric motor. The voltage and torque equations of WFSM are used to analyze the motor characteristic. Since computation via the equations is quite fast compared to FEA, this method is suitable for iterative process. The maximum efficiency oriented-characteristic analysis of the WFSM is explained in detail as follows. First, through the optimization method [69], the current condition (I_a, β, I_f) is decided to maximize the efficiency considering the voltage, current limit, and desired operating point. At this point, the interpolated values based on this LUTs are used.

Maximize:

$$\eta = \frac{P_{out}}{P_{in}} = \frac{P_{out}}{P_{out} + P_{loss}} \tag{15}$$

Subject to:

$$\begin{aligned} &T_{shaft} = p\left[\left(L_f I_f i_{oq}\right) + \left(L_d - L_q\right) i_{od} i_{oq}\right] - \left(\frac{P_{mech}}{\omega_m}\right) = T_{target} \\ &V_a = \sqrt{v_d^2 + v_q^2} \le V_{limit} = \frac{V_{dc}}{\sqrt{3}} \\ &I_a = \sqrt{i_d^2 + i_q^2} \le I_{a\_limit} \\ &I_f \le I_{f\_limit} \end{aligned} \tag{16}$$

Thereafter, the motor characteristics are predicted using the current condition determined previously. This procedure is performed by solving the d, q-axis voltage equation, and the torque equation of the WFSM, as expressed in (9)-(14). As a result, the motor characteristic that satisfies the maximum efficiency is determined. To accurately evaluate the performance of the electric motor, the circuit parameters must be accurately calculated by considering all the load conditions. To calculate the circuit parameters in each equation, the flux linkage by the field winding, d, q-axis inductance, and iron loss under the load conditions are determined via a nonlinear FEA and an analytical method. Section 4 describes the analysis methods for the circuit parameters and losses.

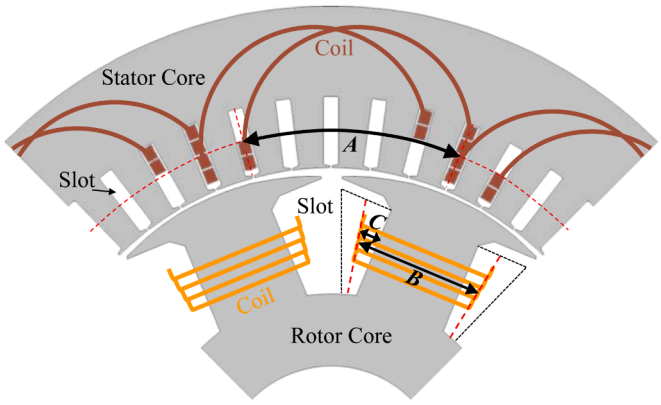

Fig. 5. Winding of the armature in the stator and the field in the rotor.

4. Analysis of circuit parameter and losses in electric motor

As described previously, the performance of the electric motor is closely related to the circuit parameters. The circuit parameters are the resistances of the field and armature coils and the inductances of the *d*- and *q*-axis equivalent circuits. In particular, an accurate loss calculation is needed to accurately calculate the efficiency of the electric motor. Fig. 4 presents the power flow of a WFSM. As shown in Fig. 4, the loss of the WFSM is classified as the copper loss of the armature and field, iron loss, and mechanical loss. This section describes the analysis methods for the circuit parameters and losses in the electric motor.

4.1. Armature & field resistance and copper losses

The end coils should be considered to accurately calculate the armature and field resistances. It is assumed that the coils of the field and armature are wound evenly inside the slot.

As shown in Fig. 5, the distributed winding is applied to the armature and the A denotes the average coil pitch of the armature coils. Therefore, the armature resistance is calculated by considering the coil pitch A and operating temperature. The resistance of the armature coil can be expressed as

$$R_a = \rho_c \cdot \frac{2\cdot(L_{stk} + \pi(A/2))\cdot N_{ph}}{A_{arm.coil}} \cdot \left[1 + \alpha\cdot\left(T_{temp} - 20^{\circ}C\right)\right] \tag{17}$$

where L_{stk} is the axial length of the core; N_{ph} is the number of series turns per phase in the armature coils; $A_{arm.coil}$ is the area of the armature coil; T_{temp} is the operating temperature in °C; ρ_c is the resistivity of the copper at 20°C; and α is the temperature coefficient of the copper. Additionally, because the alternating current (AC) flows through the armature coil, the AC resistance considering the skin and proximity effects is calculated [70, 71].

The field coils are wound around each tooth for each pole. The average coil pitch, *B*, of the field coils and the end coil height, *C*, are shown in Fig. 5. The resistance of the field coil is derived as follows:

$$R_f = \rho_c \cdot \frac{2\cdot(L_{stk} + B + 2C)\cdot N_f}{A_{fid.coil}} \cdot \left[1 + \alpha\cdot\left(T_{temp} - 20^{\circ}C\right)\right] \tag{18}$$

where N_f is the number of turns in the field coils and $A_{fld.coil}$ is the area of the field coil.

Using the resistances calculated above, the copper loss of the armature and field P_c is calculated as follows:

$$P_c = \frac{3}{2} I_a^2 R_a + I_f^2 R_f \tag{19}$$

The current of the field and armature is determined for maximizing the efficiency. The current control strategy is described in Section 3.

4.2. Iron loss and its equivalent resistance

An accurate calculation of the iron loss is important to precisely estimate the characteristics and efficiency of the electric motor [36, 37]. Fig. 6 shows the calculation process for the iron loss using the FEA. The process comprises seven steps, and the iron loss is calculated according to the magnitude and phase angle of the armature current, and the magnitude of the field current. The harmonics in the magnetic flux density in the radial and tangential components are taken into account up to the 30th order. The corresponding process is as follows:

Step 1. Using the nonlinear FEA, the radial and tangential components of the magnetic flux density are calculated for each element for one period of the electrical angle.
Step 2. The magnetic flux density calculated in Step 1 is decomposed into the magnitude according to the harmonic order through a harmonic analysis.
Step 3. Using the harmonic order obtained from step 2 and the poles of the motor, the frequency for each rotational speed is calculated.
Step 4. From the iron loss data according to the frequency and magnetic flux density of the material, the iron loss corresponding to the magnitude and frequency of each harmonic magnetic flux density is determined, considering the rotational speed. At this time, the iron loss data according to the frequency and magnetic flux density are experimentally measured using Epstein frame in accordance with the IEC60404–2 standard [72].
Step 5. In each element, the iron losses for each harmonic order are added.

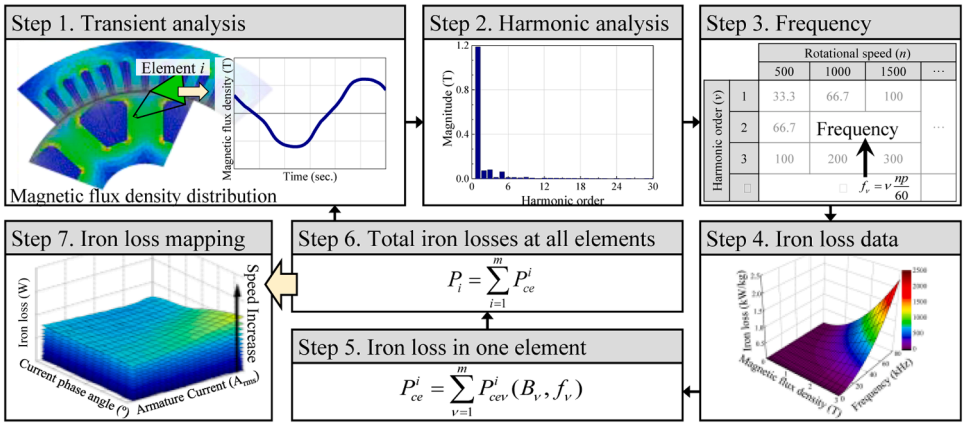

Fig. 6. Process of the iron loss calculation.

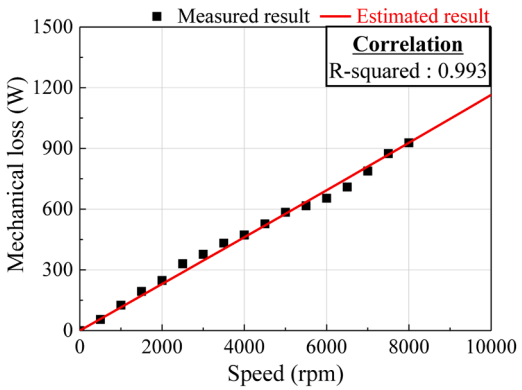

Fig. 7. Mechanical loss of the prototype.

Table 3
Design Specification for Electric Motor.

Items		Prototype	Target	Unit
Motor type		WFSM		–
Max. Power		120		kW
Max. torque / speed		280 / 10,000		Nm / rpm
Outer diameter / axial length		215 / 128		mm
Weight		44.6		kg
DC link voltage		360		V
Cooling method		Water-cooled		–
Stator (Armature)	Max. current	442.5	< 450	A_{rms}
	Max. current density	25	< 25	A_{rms}/mm^2
Rotor (Field)	Max. current	14.5	< 14	A
	Max. current density	20.5	< 20	A/mm^2

Step 6. The iron losses of all the elements are summed to determine the total iron loss of the electric motor.
Step 7. The current conditions of the field and armature are modified, and the process is repeated from Step 1. Finally, the iron loss is mapped according to the current and speed conditions.

As the speed increases, the iron loss increase. Next, using the iron loss P_i and (20), the equivalent resistance of the iron loss R_c, can be calculated, and the calculated equivalent resistance of the iron loss is applied to (9)-(14) for the performance calculation.

$$R_c = \frac{V_o^2}{P_i} = \frac{\omega^2\left\{\left(L_d i_{od} + L_f I_f\right)^2 + \left(L_q i_{oq}\right)^2\right\}}{P_i} \tag{20}$$

4.3. Inductance in d- and q- Axis Equivalent circuits

The *d*- and *q*- axis inductances and flux linkages are calculated based on a vector diagram representing the relationship between the circuit parameters and voltage equation as a vector. The related equations are as follows [73]:

$$L_d = \frac{\Psi_o \cos\delta - \Psi_a}{i_{od}} = \frac{\Psi_{od} - \Psi_a}{i_{od}} \tag{21}$$

$$L_q = \frac{\Psi_o \sin\delta}{i_{oq}} = \frac{\Psi_{oq}}{i_{oq}} \tag{22}$$

$$L_f = \frac{\Psi_a}{I_f} \tag{23}$$

where Ψ_o is the flux linkage due to the field and armature winding, Ψ_a is the flux linkage due to the field winding, and δ is the load angle.

For calculating the *d*-axis inductance, the *d*-axis flux linkage must be separated into the components by the field and armature windings. Thus, the *d*-axis inductance is obtained from the vector diagram and the incremental inductance [74]. Also, the flux linkage by the field winding is separated using the calculated *d*-axis inductance.

$$L_d = \frac{\Psi_{od2} - \Psi_{od1}}{i_{od2} - i_{od1}} \tag{24}$$

$$\Psi_a = \Psi_{od} - L_d i_{od} \tag{25}$$

Depending on the load conditions, the flux linkage due to the field and armature windings is obtained via the nonlinear FEA, and the inductances and flux linkage due to the field winding are calculated using (22)-(25).

4.4. Mechanical loss

The mechanical loss of the electric motor, including its bearing and windage friction losses, is obtained via a no-load test. This is because it is extremely difficult and time-consuming to accurately calculate the mechanical loss using the analytical method or FEA. In experimental setup, the load motor, torque sensor, and electric motor are connected mechanically in series. By driving the load motor, the rotational speed and torque are measured using a tachometer and torque sensor, respectively. The mechanical loss is calculated by multiplying the torque by the rotational speed of the electric motor under the no-load condition. During the test, as the iron core of the WFSM in the no-load condition without any electrical input is not magnetized, there is no iron loss. Therefore, the mechanical loss, including the bearing and windage friction loss of the prototype is measured via a no-load test [64]. The shaft, brush, slip ring, and bearing of the improved motor are identical to those of the prototype. Therefore, the mechanical loss of the prototype obtained from the no-load test can be used to design the improved motor. To evaluate the mechanical loss of the improved motor, based on the measured mechanical loss of the prototype, it is fitted with a polynomial function as follows [75–77]. At this time, the R-squared is presented to confirm the goodness of fit.

$$\begin{aligned} &P_{mech} = c_1 \cdot n + c_2 \cdot n^2 + c_3 \cdot n^3 \\ &\left\{c_1 = 0.1151,\ \ c_2 = 2.934 \times 10^{-14},\ \ c_3 = 1.375 \times 10^{-11}\right. \end{aligned} \tag{26}$$

where n is the rotational speed of the rotor in rpm.

The mechanical loss is estimated via (26) and used to calculate the shaft torque and efficiency of the improved motor. Fig. 7 shows the measured and estimated mechanical loss. The R-squared between these values is 0.9 or more, so it is fitted properly.

5. Improved design

5.1. Analysis of prototype with driving cycle

A performance of the prototype is evaluated through a simulation using the proposed mathematical model and calculation method for the circuit parameters and losses of the electric motor. At this time, the performance of the electric motor is affected by the magnetic properties of the iron core. The iron cores of the stator and rotor are composed of laminated electric steel sheets with low hysteresis loss. Here, the reason for stacked electrical steel sheets is to minimize eddy current loss. The material of the electric steel sheets is 35PN230 with a thickness of 0.35 mm and isotropic property. The design specifications for the electric motor considering the characteristics of the prototype as well as the specification of inverter and battery are presented in Table 3.

The maximum current density of the improved motor is determined based on that of the prototype considering the cooling method and thermal characteristics. The power density and weight are evaluated considering the iron core, as well as other parts, such as the armature and field coils, bearing, brush, and slip ring. Fig. 8 shows the efficiency and loss maps with the driving cycle under the MTPA control. As mentioned previously, the MTPA control determines the minimum

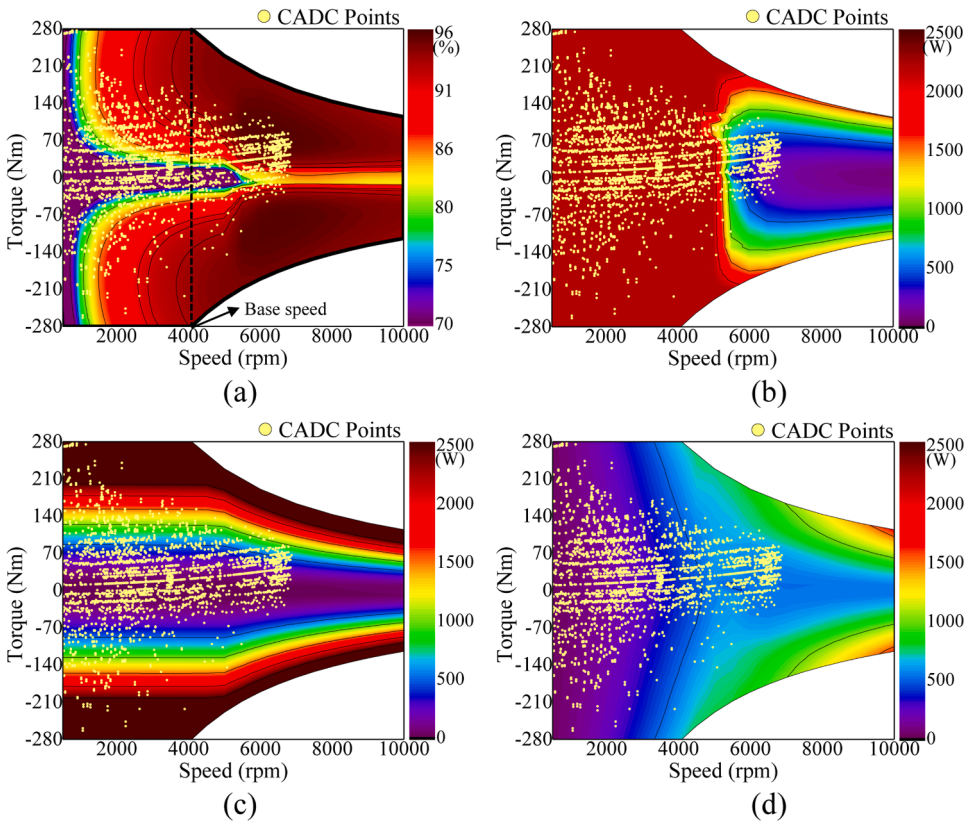

Fig. 8. Efficiency and loss map of the prototype with the driving cycle. (a) Efficiency, (b) Field copper loss, (c) Armature copper loss, (d) Iron loss.

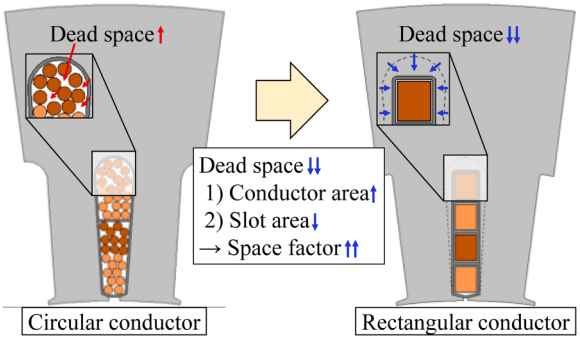

Fig. 9. Space factor according to conductor shape.

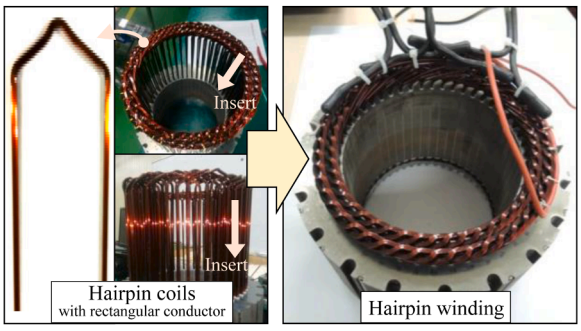

Fig. 10. Hairpin winding of the stator.

armature current that satisfies the target torque. First, as shown in Fig. 8 (a), when considering the driving cycle, the electric motor mainly operates in the region below the base speed. However, the efficiency in this region is lower than that in the high-speed region. As shown in Fig. 8 (b), there is a large field copper loss at a low speed. This is because a large field current is applied to minimize the armature current during MTPA control. Thus, the WFSM's degree of freedom is not utilized. However, as the speed increases, the current condition is determined, considering the voltage limitation. A large field current result in a large *d*-axis current, which cause increase in an armature current. Therefore, the field current is gradually reduced by the MTPA control and exhibits the same trend as the field copper loss. Additionally, as shown in Fig. 8 (c) and (d), as the torque increases, the armature copper loss increases, and as the speed increases, the iron loss increases. However, when the driving cycle is considered, the iron loss is relatively low. Therefore, as the major loss under the driving cycle is the copper loss, the design direction and control method for improving the efficiency considering the driving cycles involve reducing the field and armature copper losses, while minimizing the increase in the iron loss.

5.2. *Armature winding and rectangular conductor*

In this study, a rectangular conductor is used to improve the efficiency. If the rectangular conductor is used, a large space factor is obtained [46–49]. The space factor is defined as the ratio of the conductor area to slot area. As shown in Fig. 9, the rectangular conductor can reduce the dead space (as indicated by the red arrow) when using a circular conductor. Therefore, it presents the following advantages.

1) An increase in the conductor area (the slot area is constant): decreases in the resistance and current density, as well as a copper loss reduction.

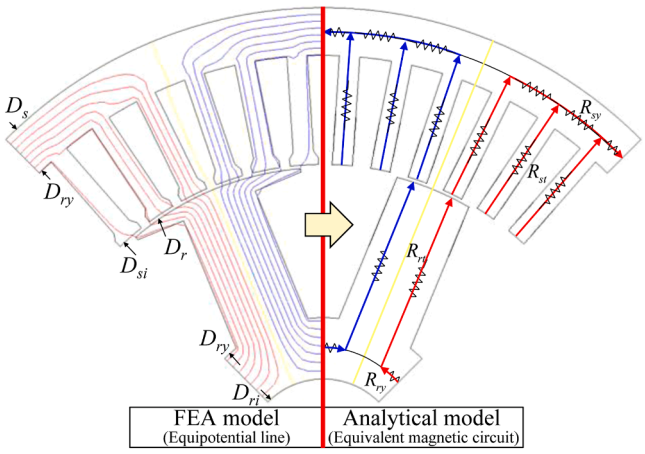

Fig. 11. Equivalent magnetic circuit and equipotential line of the simplified model.

2) A decrease in the slot area (the conductor area is constant): increases in the widths of the teeth and yoke, as well as magnetic flux density and iron loss reduction

Also, the hairpin winding with a rectangular conductor is used for the armature winding. The hairpin winding is formed by inserting hairpin coils with the rectangular conductor into the stator slots and welding the hairpin coils together. This process is shown in Fig. 10. Because the hairpin coils are inserted into the stator slots after they are formed, the manufacturing process is simple, and the end coil height is uniform. Moreover, the cooling performance and the breakdown voltage between the coils are excellent [48, 49]. However, this method results in a weight increase owing to the large space factor. Furthermore, because the hairpin winding is structurally complex, it is difficult to use the parallel circuit and strands [47]. Therefore, in Section 5.4, these disadvantages are considered in the design.

5.3. Core shape of rotor and stator

The tooth and yoke widths of the rotor and stator are determined to minimize the reluctance of the rotor and stator core. The smaller reluctance of the core yields a greater the magnetic flux at the same current. Thus, the minimum reluctance results in the minimum current for generating the torque, which can reduce the copper loss. The reluctance of the rotor and stator are calculated using an equivalent magnetic circuit (EMC). The EMC provides an effective analytical method for identifying the trends at the design stage owing to its short-computational time [15, 44, 78].

The assumptions used in the EMC are as follows:

1) EMC is supposed 2-D and end-effects are neglected.
2) Eddy-current and hysteresis effects are ignored.
3) Magnetic materials are considered as isotropic.
4) Effective magnetic flux path is considered as the average magnetic flux path.
5) Leakage magnetic flux is neglected.
6) Tooth tips of the rotor and stator are ignored.
7) Surface of the stator core is smooth.
8) Magnetic flux paths in the EMC consist of line segments and circular arcs.

The average magnetic flux path must be determined to construct the EMC. The equipotential lines indicating the magnetic flux paths are shown on the left side of Fig. 11.

The field coils in the rotor are concentrated on one tooth. The magnetic flux through the tooth is divided into two sides of the yoke, and the divided magnetic flux passes to the next tooth. However, the distributed winding is applied to the armature coils in the stator. Thus, the magnetic flux divided into the two sides of the yoke past the teeth flows into the teeth on the opposite pole. The EMC based on these magnetic flux paths is shown on the right side of Fig. 11. Before calculating the reluctance of the constructed circuit, the relationship between the width of the teeth and that of the yoke in the rotor and stator is as follows. Therefore, the yoke widths of the stator and rotor are determined by the tooth width of those.

$$w_{ts} = 2 \cdot x_s, \quad w_{ys} = \frac{D_s - D_{sy}}{2} \tag{27}$$

$$w_{tr} = 2 \cdot x_r, \quad w_{yr} = \frac{D_{ry} - D_{ri}}{2} \tag{28}$$

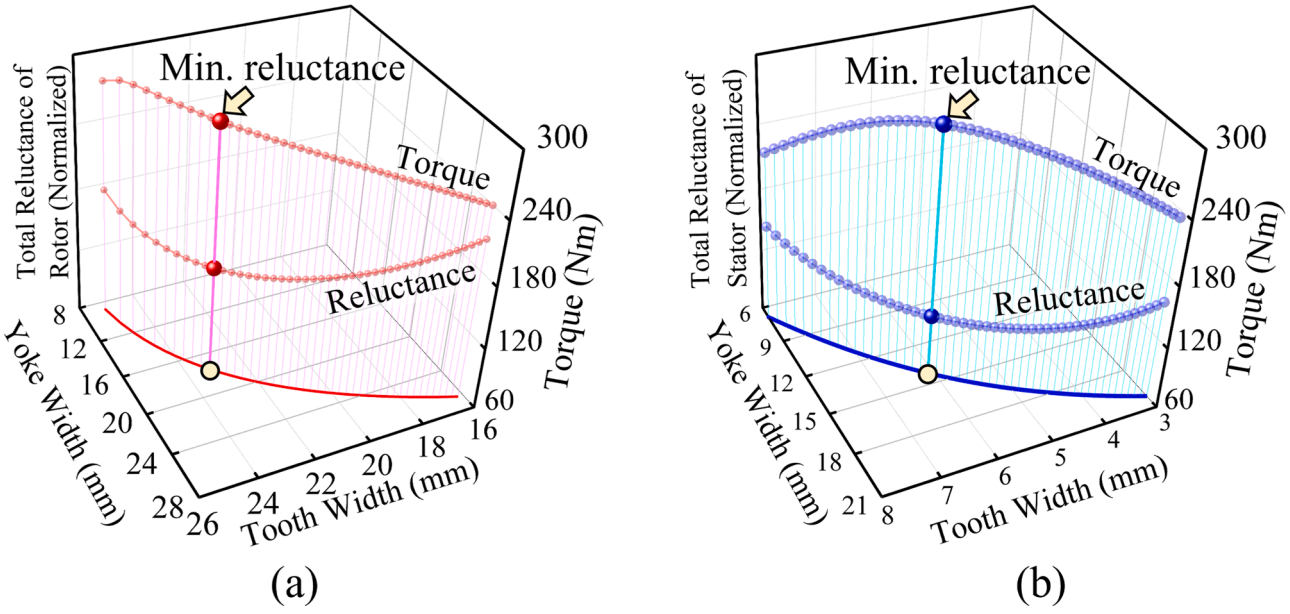

Fig. 12. Total reluctance and torque according to the tooth and yoke widths of the improved motor. (a) Rotor, (b) Stator.

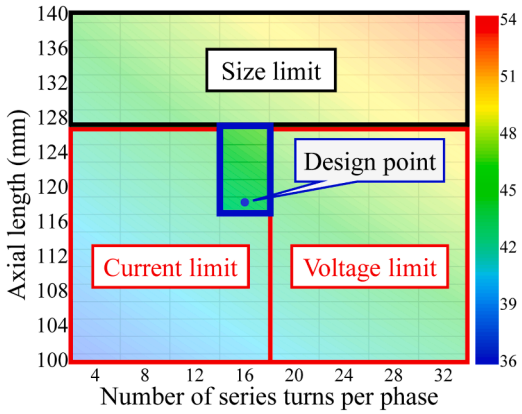

Fig. 13. Weight of the improved motor according to the axial length and number of series turns per phase.

Table 4
Material Properties for Structural Analysis.

	Copper	Electric steel sheet	Retainer	Shaft	Unit
Density (Equivalent density)	8940 (4100)	7600	1300	8000	Kg/m^3
Young's modulus	128	175	3.7	193	GPa
Poisson's ratio	0.36	0.3	0.38	0.27	–
Yield strength	100	380	80	250	MPa

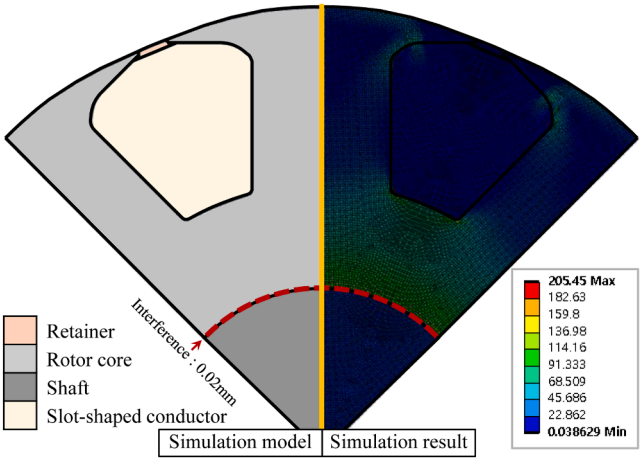

Fig. 14. Structural analysis for the improved motor at 10,000 rpm.

$$D_{ry} = \frac{2s_{rn}x_r}{\pi} + \sqrt{\left(\frac{2s_{rn}x_r}{\pi}\right)^2 + D_{ri}^2 - \frac{4s_{rn}}{\pi}(x_r D_{ri} + A_r)} \tag{29}$$

$$D_{sy} = \frac{2s_{sn}x_s}{\pi} + \sqrt{\left(\frac{2s_{sn}x_s}{\pi}\right)^2 + D_s^2 - \frac{4s_{sn}}{\pi}(x_s D_s - A_s)} \tag{30}$$

where w_{ts} and w_{ys} are the width of the tooth and yoke in the stator, respectively; w_{tr} and w_{yr} are the width of the tooth and yoke in the rotor, respectively; D_s is the outer diameters of the stator; D_{sy} is the inner diameter of the stator yoke; D_{ry} is the outer diameter of the rotor yoke; D_{ri} is the inner diameters of the rotor; x_s and x_r are the half tooth widths of the stator and rotor, respectively; s_{sn} and s_{rn} are the numbers of stator and rotor slots, respectively; A_s and A_r are the slot areas of the stator and rotor, respectively;

Finally, the reluctance of the constructed circuit is calculated as

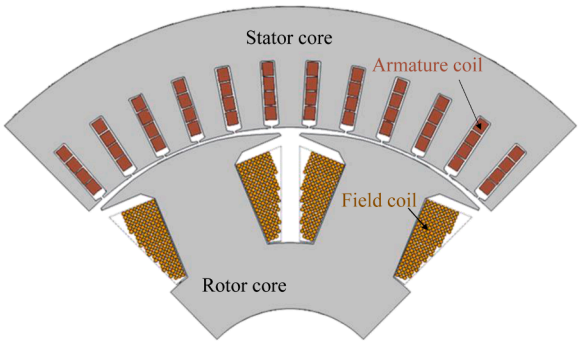

Fig. 15. The configuration of the improved motor as the proposed design.

follows:

$$R_{rm} = 2R_{rt} + R_{ry} \tag{31}$$

$$R_{sm} = 2\frac{R_{st}^3 + 3R_{st}^2R_{sy} + R_{st}R_{sy}^2}{3R_{st}^2 + 4R_{st}R_{sy} + R_{sy}^2} + R_{sy} \tag{32}$$

where

$$R_{rt} = \frac{2D_r - D_{ry} - D_{ri}}{8\mu x_r L_{stk}},\ R_{ry} = \frac{\pi(D_{ry} + D_{ri}) - 2x_r s_{rn}}{\mu s_{rn} L_{stk}(D_{ry} - D_{ri})} \tag{33}$$

$$R_{st} = \frac{D_{sy} + D_s - 2D_{si}}{8\mu x_s L_{stk}},\ R_{sy} = \frac{\pi(D_{sy} + D_s)}{\mu L_{stk}(D_s - D_{sy})} \tag{34}$$

where D_r is the outer diameters of the rotor; D_{si} is the inner diameters of the stator; L_{stk} is the axial length of the core; μ is the permeability of the stator and rotor core; D_{si} is determined by the rotor diameter D_r and the air-gap lengths.

The calculated reluctance and torque, which vary with respect to the tooth and yoke widths of the rotor and stator cores, are shown in Fig. 12. At this time, the yoke width according to the teeth width was determined by (27)-(30) and expressed as a line on the x-y plane. Also, the torque is obtained through FEA under the maximum current condition. Finally, the tooth and yoke widths of the rotor and stator cores are determined as the minimum points of the reluctance R_{sm} and R_{rm} of the electric motor. Thus, the tooth and yoke widths of the stator are determined at the maximum torque point. The tooth and yoke widths of the rotor are determined at a torque point that differed from the maximum torque by 1%.

5.4. Number of series turns per phase for armature winding and axial length of core

In the previous step, the stator and rotor core shapes of the improved motor were determined. Next, it is necessary to determine the axial length. As previously discussed, the use of rectangular conductors increases the weight of the electric motor. Therefore, in consideration of the weight, the axial length and number of series turns per phase of the armature winding must be determined. Decreases in the axial length and number of series turns per phase of the armature winding requires a larger input current to generate the same torque, owing to the decrease in the flux linkage. Conversely, increases in the axial length and number of series turn per phase of the armature winding requires a higher input voltage, because of the increases in the armature resistance, inductance, and flux linkage. Fig. 13 shows the weight change of the electric motor according to the axial length and number of series turns per phase of the armature winding. The red line box indicates a region that does not satisfy the output power within a given input voltage and current limit. The black line box indicates the region where the axial length is greater than that of the prototype. This region requires additional space in the

Table 5
Design Parameters.

Items		Prototype	Improved motor	Target	Unit
Motor type		WFSM			–
Conductor type		Circular (Conventional)	Rectangular (Hairpin)	–	
Max. Power		120			kW
Max. torque / speed		270 / 10,000			Nm / rpm
DC link voltage		360			V
Axial length		128	118 (−7.8%)	–	mm
Weight		44.6	44 (−1.3%)	< 45	kg
Stator (Armature)	Outer diameter	215			mm
	Max. current	442.5	446.3	< 450	A_{rms}
	Max. current density	25.0	22 (−12%)	< 25	A_{rms}/mm^2
	Series turn per phase	16		–	–
	Tooth/Yoke width	6.4 / 12.5	6.1 / 14.2	–	mm
Rotor (Field)	Outer diameter	149		–	mm
	Max. current	14.5	13.5	< 14	A
	Max. current density	20.5	19.0 (−6.9%)	< 20	A/mm^2
	Turn per pole	155	145	–	–
	Tooth/Yoke width	21.5 / 16.5	23 / 17.6	–	mm

Table 6
DC Resistance of Prototype and Improved Motor.

Items		Prototype	Improved motor	Unit
Field resistance	Estimated value	10.13	8.73	Ω
	Test	9.57	8.46	
	Error	5.9	2.0	%
Armature esistance	Estimated value	6.73	5.57	mΩ
	Test	6.68	5.46	
	Error	0.7	3.2	%

vehicle system owing to an increase in the axial length. Therefore, it is excluded from the design point. The blue line box excluding these two regions is a region that satisfies the output power within a limited space, voltage, and current. The axial length and number of series turns per phase of the armature winding satisfying the minimum weight are selected in this region. Thus, to minimize the weight of the electric motor, the axial length of the improved motor is determined to be 118 mm, and the number of series turns per phase of the armature windings is determined to be 16.

5.5. Structural analysis

A structural analysis of the rotor core with the conductor and retainer in the improved motor is conducted to confirm the structural stability. The simulation is performed at maximum speed of 10,000 rpm via 2D FEA using the ANSYS workbench. The material properties of the rotor components are presented in Table 4.

The field coil is modeled as a slot-shaped conductor [25, 79]. An equivalent density is applied to the slot-shaped conductor to consider the weight of the field coil including the end coil. Here, the equivalent density is calculated by dividing the weight of the field coil by the volume of the slot ($V_{slot}=A_rL_{stk}$). The shaft is manufactured by shrink-fitting it into the rotor core. At this time, the interference between the shaft and the rotor core is 0.02 mm as in the prototype, and this condition is reflected in the simulation [80]. The simulation model and result are shown in Fig. 14. The maximum stress is approximately 205 MPa. Thus, an improved motor with a safety factor of 1.85 is structurally stable. Finally, the configuration of the improved motor resulting from the proposed design is shown in Fig. 15. As a result, the design parameters of the prototype and the improved motor are presented in Table 5. The axial length of the improved motor (118 mm) is 7.8% smaller than that of the prototype (128 mm).

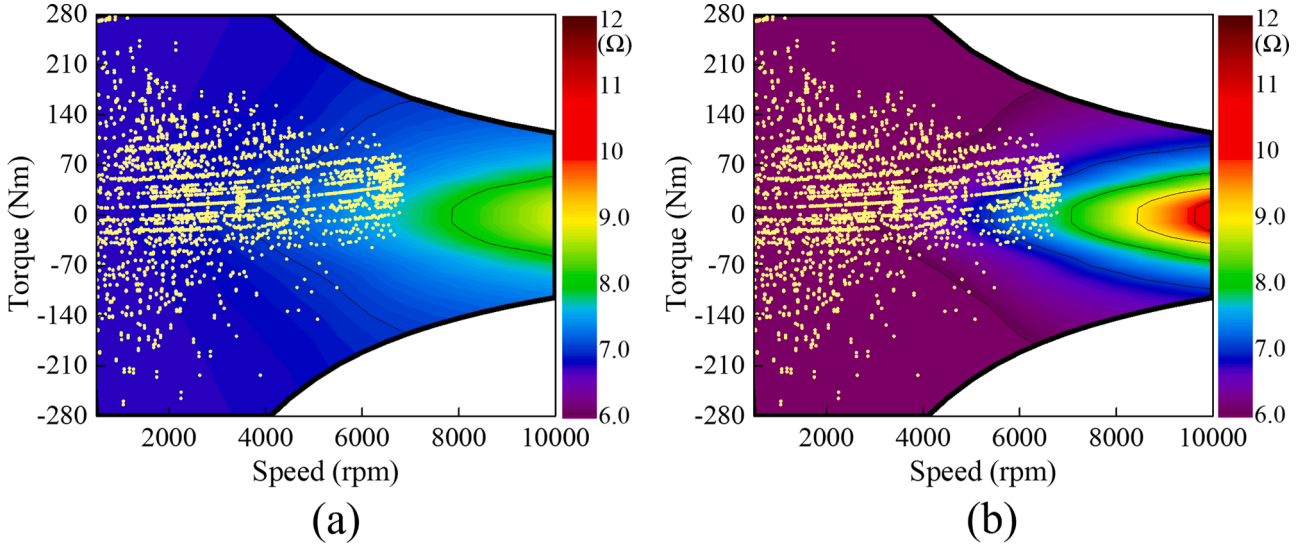

Fig. 16. AC resistance according to the analysis model. (a) Prototype, (b) Improved motor.

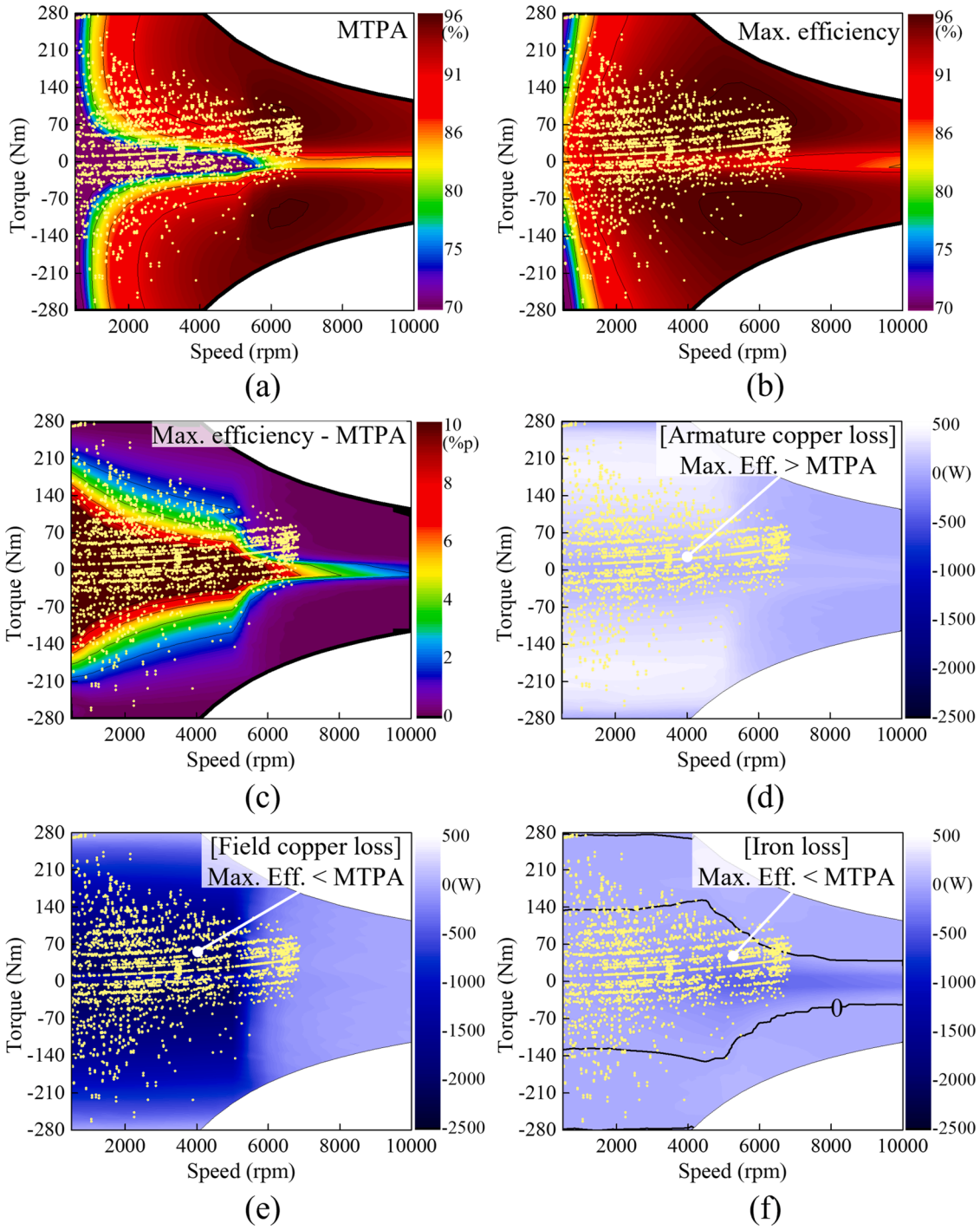

Fig. 17. Efficiency and loss difference maps of the improved motor according to current vector control. (a) Efficiency under MTPA control, (b) Efficiency under maximum efficiency control, (c) Efficiency difference, (d) Armature copper loss difference, (e) Field copper loss difference, (f) Iron loss difference.

6. Design results and verification

6.1. Performance of electric motor

The performance of the electric motor is analyzed using the previously proposed circuit parameter, loss analysis and control methods. The iron loss, flux linkage, and inductance are calculated and mapped according to the current conditions. These circuit parameters are mapped for field currents of 0 to 14A, armature currents of 0 to 450A_{rms}, armature current phase angles of −30° to 90°, and rotational speed of 0 to 10,000rpm.

The calculated and measured DC resistances of the prototype and improved model are presented in Table 6. Also, Fig. 16 shows the AC resistance of the prototype and the improved motor. The conductor area of the improved motor is larger than that of the prototype. Although the DC resistance of the improved motor is lower than that of the prototype, the AC resistance of the improved motor increases significantly as the speed increases, owing to the skin and proximity effects.

Next, the efficiency of the improved motor according to the current vector control method is analyzed. Fig. 17(a) and (b) show the efficiency maps according to the current vector control method, and Fig. 17(c) shows the difference between them. The efficiency increases in all

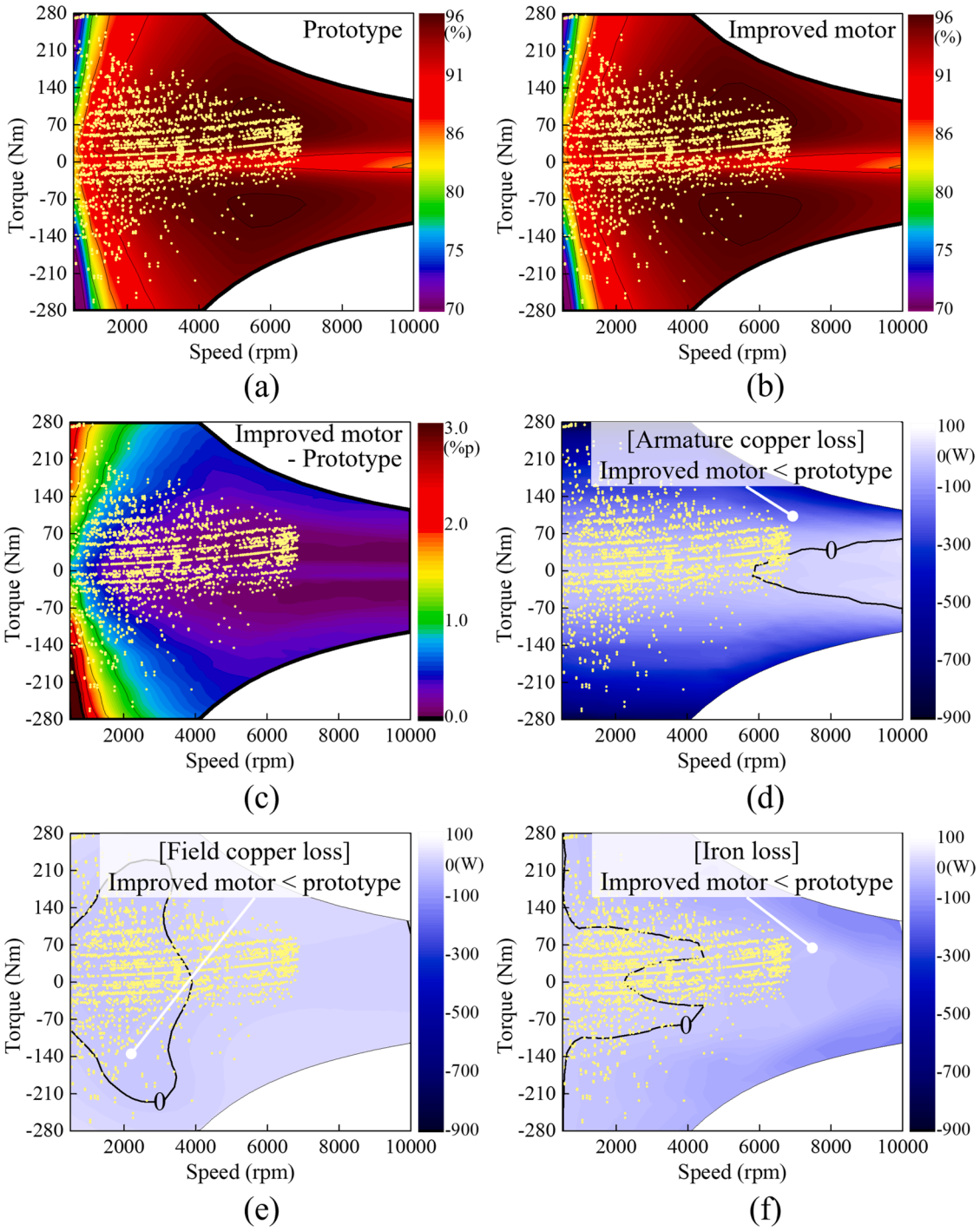

Fig. 18. Efficiency and loss difference maps of the prototype and improved motor. (a) Efficiency of the prototype, (b) Efficiency of the improved motor, (c) Efficiency difference, (d) Armature copper loss difference, (e) Field copper loss difference, (f) Iron loss difference.

regions under the maximum efficiency control. The efficiency increase is particularly large in the low-speed region. As shown in Fig. 17(d), the armature copper loss is small under the MTPA control considering only the armature current. However, as shown in Fig. 17(e), the field loss when the maximum efficiency control is applied is smaller than the field loss when the MTPA control is applied. In the low-speed region, the maximum efficiency control requires a small field current, in contrast to the MTPA control, which increases the field current to satisfy the torque while minimizing the armature current. However, as the speed increases, the MTPA control also reduces the field current owing to the voltage limitation; thus, the difference in field copper losses between the control methods is reduced. For this reason, in the low-speed region, the field copper loss significantly depends on the control method. Thus, the proposed maximum efficiency control considering all the losses, including the field copper loss, is more effective for improving the efficiency than the MTPA control, which minimizes only the armature copper loss. Additionally, the field current is flexibly controlled during maximum efficiency control.

Finally, the efficiencies of the prototype and improved motor are analyzed. Fig. 18 shows the results of applying the maximum efficiency control to the prototype and the improved motor to verify the effectiveness of the proposed design method. Fig. 18(a) and (b) show the

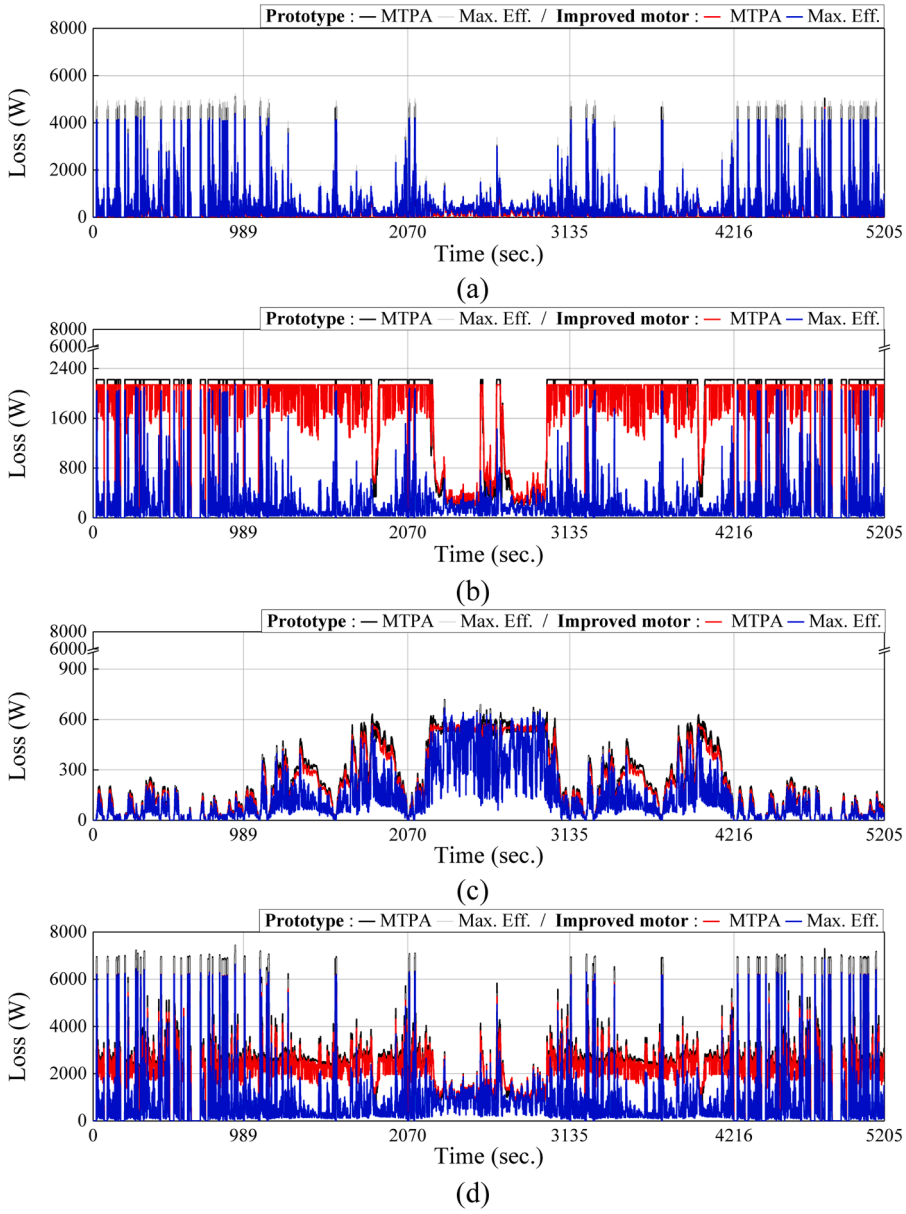

Fig. 19. Losses over time for the prototype and improved motor. (a) Armature copper loss, (b) Field copper loss, (c) Iron loss, (d) Total loss.

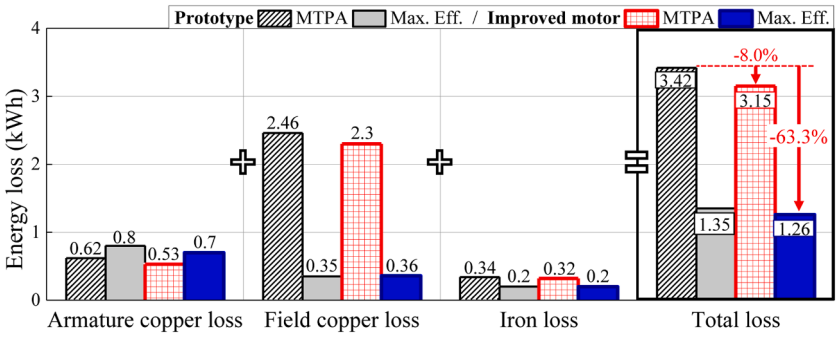

Fig. 20. Energy losses of the prototype and improved motor.

efficiency maps of both electric motors, and Fig. 18(c) shows the difference between them. The efficiency of the improved motor increases in all regions. As described previously, the proposed design method can reduce the armature copper loss. As shown in Fig. 18(d), (e), and (f), the losses of the prototype are smaller than those of the improved motor in some regions. However, the total loss of the improved motor is smaller than that of the prototype in all the regions. Therefore, the proposed design method and control strategy are effective for improving the

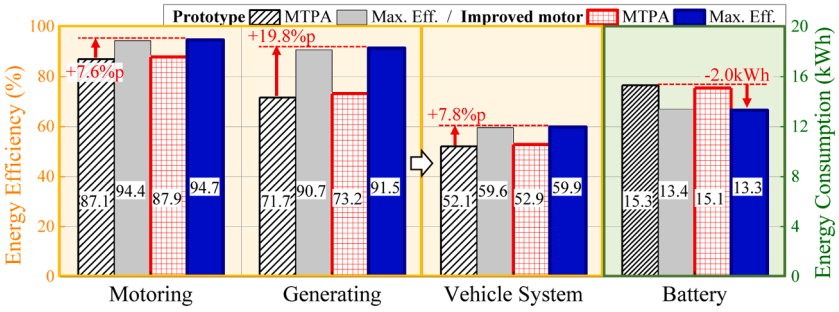

Fig. 21. Performance of the electric motor and vehicle considering the driving cycle.

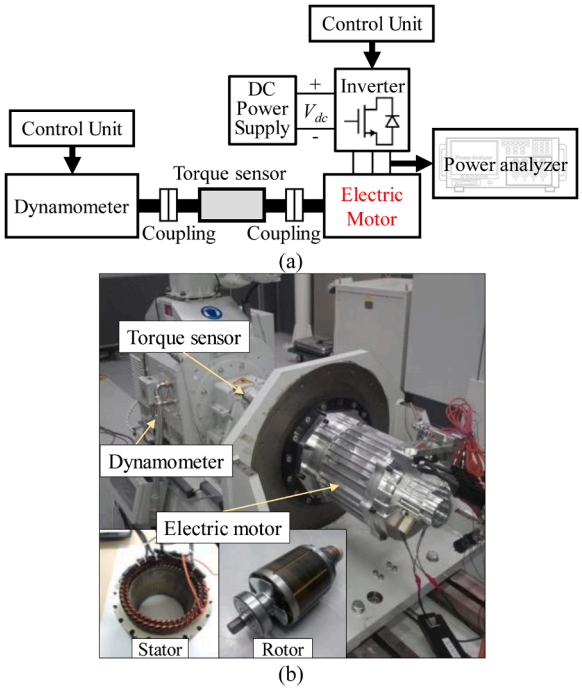

Fig. 22. Load test. (a) schematic, (b) test setup.

efficiency of the WFSM.

6.2. Performance of vehicle system with driving cycle

The performance of the EV applying the two aforementioned electric motors is analyzed. A simulation is performed using the ADVISOR software. Fig. 19 shows the losses of the electric motors (i.e., the prototype and improved motor) when the target vehicle is driven along the driving cycle. Also, Fig. 20 shows the evaluated energy loss based on the loss over time.

Under the same MTPA control conditions, the total loss of the improved motor is smaller than that of the prototype. Owing to the proposed design method, the energy loss caused by the armature copper loss is reduced by approximately 14%. Consequently, the total energy loss decreases by 8%, as shown in Fig. 20. Comparing the energy loss of the two motors based on the maximum efficiency control, the same trend is observed. In addition, applying the proposed maximum efficiency control increases the armature loss rather than the MTPA control which only minimizes the armature current, but all the other losses are reduced, particularly the field copper loss. Because of this effect, the total energy loss is reduced by 63.3%.

Based on these results, the energy efficiencies of the motoring and generating operation modes of the two electric motors, as well as that of a vehicle system applying the two electric motors are shown in Fig. 21. At this time, for the EV system simulation, the specifications of other components presented in Table 1 are applied. When the proposed design method and control strategy are applied, the energy efficiencies of the two operating modes are increased by 7.6%p and 19.8%p, respectively. By applying the proposed methods, the energy efficiency of the vehicle system is increased by 7.8%p. Additionally, the energy consumption of the battery is reduced by 2.0kWh.

6.3. Verification

To verify the validity of the proposed methods, a load test of the prototype and improved motor is set up and conducted. Fig. 22 shows a schematic and the setup of the load test. The electric motor is mechanically connected to the torque sensor and dynamometer in series. The efficiency is measured at speeds in the range of 1000rpm to 10,000rpm and torques in the range of 20Nm to 280Nm. The control method for these motors is the maximum efficiency control. Fig. 23 and Fig. 24

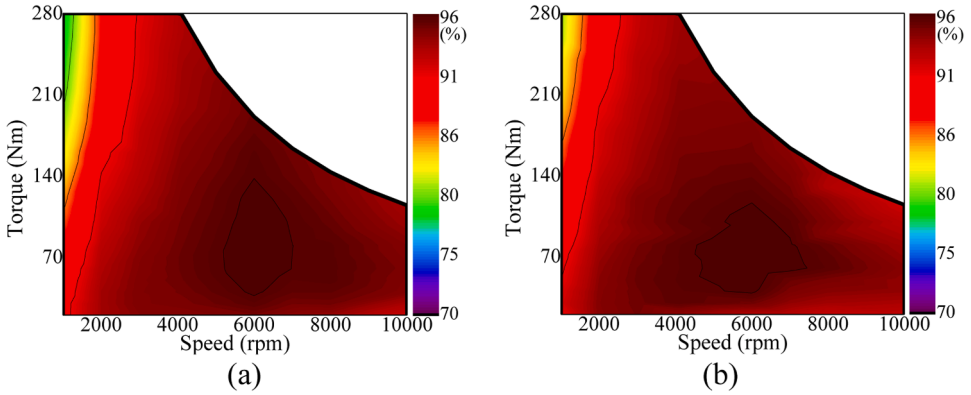

Fig. 23. Test results. (a) Prototype, (b) Improved motor.

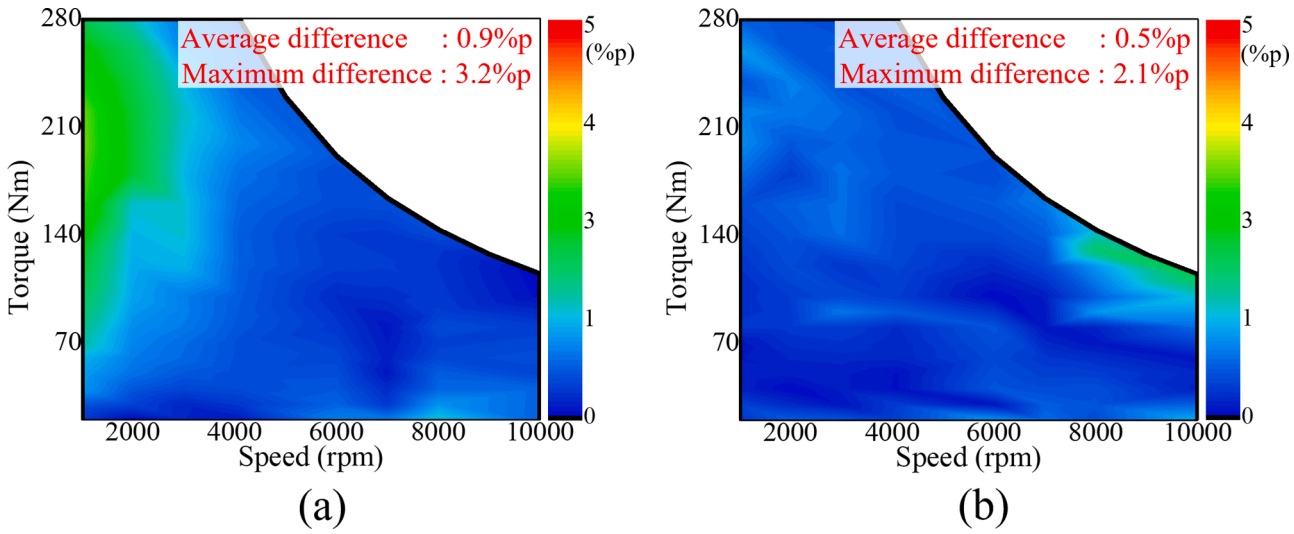

Fig. 24. Difference between the simulation and test results. (a) Prototype, (b) Improved motor.

present the test results and a comparison between the simulation and test results. The average difference in efficiency between the simulation and test of the prototype is 0.9%p, and that of the improved motor is 0.5%p. Also, the maximum difference in the efficiency between the simulation and test of the prototype is less than 3.2%p, and that of the improved motor is less than 2.1%p. Therefore, the proposed methods are validated.

7. Conclusion and future work

In this paper, the methods for improving and estimating the energy efficiency of an EV applying the WFSM were proposed. The contributions of this paper are 1) an EV model considering the electric motor, 2) a control strategy for the WFSM to increase the energy efficiency, 3) analysis methods for the circuit parameters and losses to accurately calculate the performance of the electric motor and vehicle system, and 4) a design process to improve the efficiency of the electric motor and the EV using the proposed methods. Using these methods, the driving points of the electric motor is calculated, and the characteristics of the vehicle system according to the characteristics of the electric motor are quantitatively evaluated. As a result, the volume of the improved motor was 7.8% smaller than that of the prototype. Additionally, the efficiency resulting from the control strategy of the improved motor is excellent in all regions. Furthermore, compared with the efficiency of the prototype, the efficiency of the improved motor using the proposed design method is superior in all regions. These electric motors were applied to an EV, and the characteristics of the EV were analyzed by considering the driving cycle. Compared with the total energy loss of the prototype, that of the improved motor applying the proposed control strategy and design method was reduced by 63.3%. Therefore, the energy efficiency of the vehicle system was increased by 7.8%p, and the energy consumption of the battery was reduced by 2.0kWh. Finally, to verify the proposed methods, efficiency tests of the fabricated prototype and improved motor were performed. As a result, the average difference in efficiency between the simulation and test were 0.9%p for the prototype and 0.5%p for the improved motor, which are reasonable. However, in this paper, to increase the energy efficiency of the EV system, the research on the electric motor is focused, and the discussion on other components in the EV system such as the power electronics and the reduction gear is insufficient. In addition, only experiments with electric motors are conducted. Therefore, in the future, The EV system with all components including the electric motor will be studied and experimentally tested based on the effectiveness of the proposed method.

Declaration of Competing Interest

None

Author statement

None

References

[1] Ruuskanen V, Nerg J, Rilla M, Pyrhönen J. Iron loss analysis of the permanent-magnet synchronous machine based on finite-element analysis over the electrical vehicle drive cycle. IEEE Trans Ind Electron 2016;63(7):4129–36.
[2] Wang J, Yuan X, Atallah K. Design optimization of a surface-mounted permanent-magnet motor with concentrated windings for electric vehicle applications. IEEE Trans Veh Technol 2013;62(3):1053–64.
[3] Feng G, Lai C, Iyer KLV, Kar NC. Improved high-frequency voltage injection based permanent magnet temperature estimation for PMSM condition monitoring for EV applications. IEEE Trans Veh Technol 2018;67(1):216–25.
[4] Estima JO, Marques Cardoso AJ. Efficiency analysis of drive train topologies applied to electric/hybrid vehicles. IEEE Trans Veh Technol 2012;61(3):1021–31.
[5] Iyer KLV, Lai C, Mukundan S, Dhulipati H, Mukherjee K, Kar NC. Investigation of interior permanent magnet motor with dampers for electric vehicle propulsion and mitigation of saliency effect during integrated charging operation. IEEE Trans Veh Technol 2019;68(2):1254–65.
[6] Sarigiannidis AG, Beniakar ME, Kladas AG. Fast adaptive evolutionary PM traction motor optimization based on electric vehicle drive cycle. IEEE Trans Veh Technol 2017;66(7):5762–74.
[7] Fatemi A, Ionel DM, Popescu M, Chong YC, Demerdash NAO. Design optimization of a high torque density spoke-type PM motor for a formula E race drive cycle. IEEE Trans Ind Appl 2018;54(5):4343–54.
[8] Dang L, Bernard N, Bracikowski N, Berthiau G. Design optimization with flux weakening of high-speed PMSM for electrical vehicle considering the driving cycle. IEEE Trans Ind Electron 2017;64(12):9834–43.
[9] Ahn K, Bayrak AE, Papalambros PY. Electric vehicle design optimization: integration of a high-fidelity interior-permanent-magnet motor model. IEEE Trans Veh Technol 2015;64(9):3870–7.
[10] Park M, Jung J, Kim D, Hong J, Lim M. Design of high torque density multi-core concentrated flux-type synchronous motors considering vibration characteristics. IEEE Trans Ind Appl 2019;55(2):1351–9.
[11] Park M, Kim H, Choi Y, Hong J, Lee J. Characteristics of IPMSM according to rotor design considering nonlinearity of permanent magnet. IEEE Trans Magn 2016;52 (3):1–4.
[12] Öksüztepe E. In-wheel switched reluctance motor design for electric vehicles by using a pareto-based multiobjective differential evolution algorithm. IEEE Trans Veh Technol 2017;66(6):4706–15.
[13] López-Torres C, Garcia Espinosa A, Riba J, Romeral L. Design and optimization for vehicle driving cycle of rare-earth-free SynRM based on coupled lumped thermal and magnetic networks. IEEE Trans Veh Technol 2018;67(1):196–205.
[14] Petrov I, Niemelä M, Ponomarev P, Pyrhönen J. Rotor surface ferrite permanent magnets in electrical machines: advantages and limitations. IEEE Trans Ind Electron 2017;64(7):5314–22.
[15] Utegenova S, et al. An investigation into the coupling of magnetic and thermal analysis for a wound-rotor synchronous machine. IEEE Trans Ind Electron 2018;65 (4):3406–16.

[16] Pellegrino G, Vagati A, Boazzo B, Guglielmi P. Comparison of induction and PM synchronous motor drives for EV application including design examples. IEEE Trans Ind Appl 2012;48(6):2322–32.
[17] Yang Z, Shang F, Brown IP, Krishnamurthy M. Comparative study of interior permanent magnet, induction, and switched reluctance motor drives for EV and HEV applications. IEEE Trans Transport Electrific 2015;1(3):245–54.
[18] Jayarajan R, Fernando N, Nutkani IU. A review on variable flux machine technology: topologies, control strategies and magnetic materials. IEEE Access 2019;7:70141–56.
[19] Zheng Y, Wu L, Fang Y, Huang X, Lu Q. A hybrid interior permanent magnet variable flux memory machine using two-part rotor. IEEE Trans Magn 2019;55(7):1–8.
[20] Athavale A, Sasaki K, Gagas BS, Kato T, Lorenz RD. Variable flux permanent magnet synchronous machine (VF-PMSM) design methodologies to meet electric vehicle traction requirements with reduced losses. IEEE Trans Ind Appl 2017;53(5):4318–26.
[21] Jain AK, Ranganathan VT. Modeling and field oriented control of salient pole wound field synchronous machine in stator flux coordinates. IEEE Trans Ind Electron 2011;58(3):960–70.
[22] Dorrell DG. Are wound-rotor synchronous motors suitable for use in high efficiency torque-dense automotive drives?. In: Proc. 38th Annu. Conf. IEEE Ind. Electron. Soc.; 2012. p. 4880–5.
[23] Kim Y, Nam K. Copper-loss-minimizing field current control scheme for wound synchronous machines. IEEE Trans Power Electron 2017;32(2):1335–45.
[24] Lim M, Hong J. Design of high efficiency wound field synchronous machine with winding connection change method. IEEE Trans Energy Convers 2018;33(4):1978–87.
[25] Di Gioia A, et al. Design and demonstration of a wound field synchronous machine for electric vehicle traction with brushless capacitive field excitation. IEEE Trans Ind Appl 2018;54(2):1390–403.
[26] Jawad G, Ali Q, Lipo TA, Kwon B. Novel brushless wound rotor synchronous machine with zero-sequence third-harmonic field excitation. IEEE Trans Magn 2016;52(7):1–4.
[27] Luong HTL, Henaux C, Messine F, Bueno-Mariani G, Voyer N, Mollov S. Finite element analysis of a modular brushless wound rotor synchronous machine. J Eng 2019;2019(17):3521–6.
[28] Liu Y, Zhang Z, Wang C, Geng W, Wang H. Electromagnetic performance analysis of a new hybrid excitation synchronous machine for electric vehicle applications. IEEE Trans Magn 2018;54(11):1–4.
[29] Hwang S, Sim J, Hong J, Lee J. Torque improvement of wound field synchronous motor for electric vehicle by PM-assist. IEEE Trans Ind Appl 2018;54(4):3252–9.
[30] Chai W, Yang H, Xing F, Kwon B. Analysis and design of a PM-assisted wound rotor synchronous machine with reluctance torque enhancement. IEEE Trans Ind Electron 2021;68(4):2887–97.
[31] Chai W, Kwon J, Kwon B. Analytical design of a hybrid-excited wound field synchronous machine for the improvement of torque characteristics. IEEE Access 2020;8:87414–21.
[32] Chai W, Zhao W, Kwon B. Optimal design of wound field synchronous reluctance machines to improve torque by increasing the saliency ratio. IEEE Trans Magn 2017;53(11):1–4.
[33] Park S, Kim K. Torque ripple reduction method with asymmetric pole for wound-field synchronous motor. IEEE Trans Magn 2015;51(3):1–4.
[34] Liu W, Lipo TA. Saliency enhancement of salient pole wound field synchronous machines for variable speed applications. In: Proc. 2017 IEEE International Electric Machines and Drives Conference (IEMDC); 2017. p. 1–7.
[35] Kim B, Kang D. A Study on the Novel Design to Improve Efficiency of Wound field Synchronous Machine. IEEE Trans Magn 2021;57(2):1–6.
[36] Rasilo P, Belahcen A, Arkkio A. Importance of Iron-Loss Modeling in Simulation of Wound-Field Synchronous Machines. IEEE Trans Magn 2018;48(9):2495–504.
[37] Rasilo P, Belahcen A, Arkkio A. Experimental determination and numerical evaluation of core losses in a 150-kVA wound-field synchronous machine. IET Electr Power Appl 2013;7(2):97–105.
[38] Jiao N, Liu W, Meng T, Sun C, Jiang Y. Decoupling start control method for aircraft wound-rotor synchronous starter-generator based on main field current estimation. IET Electr Power Appl 2013;13(7):863–70.
[39] Uzel D, Peroutka Z, Smldl V, Kosan T, Zeman K. Self-Sensing Control of Wound Rotor Synchronous Motor Drive for Mine Hoist. IEEE Trans Ind Electron 2018;65(3):2009–17.
[40] Meng T, Liu W, Han X, Jiao N, Peng J, Jiang Y. Multi-Stage-Structure-Based Rotor Position Estimation for a Wound-Field Synchronous Starter Generator in the Low-Speed Region. IEEE Trans Power Electron 2019;34(12):12095–105.
[41] Jiao N, Liu W, Zhang Z, Meng T, Peng J, Jiang Y. Field Current Estimation for Wound-Rotor Synchronous Starter–Generator With Asynchronous Brushless Exciters. IEEE Trans Energy Convers 2017;21(4):1554–61.
[42] Hwang D, Gu B. Field Current Control Strategy for Wound-Rotor Synchronous Motors Considering Coupled Stator Flux Linkage. IEEE Access 2020;8:111811–21.
[43] Nie Y, Brown IP, Ludois DC. Deadbeat-Direct Torque and Flux Control for Wound Field Synchronous Machine. IEEE Trans Ind Electron 2018;65(3):2069–79.
[44] Park H, Lim M. Design of high power density and high efficiency wound-field synchronous motor for electric vehicle traction. IEEE Access 2019;7:46677–85.
[45] Park M, Kim D, Jung Y, Lim M, Hong J. Modeling, Design and Control of Wound-Field Synchronous Motor for High Energy Efficiency of Electric Vehicle. In: Proc. IEEE Energy Convers. Congr. Expo. (ECCE); 2019. p. 3960–7.
[46] Popescu M, Goss J, Staton DA, Hawkins D, Chong YC, Boglietti A. Electrical vehicles—practical solutions for power traction motor systems. IEEE Trans Ind Appl 2018;54(3):2751–62.
[47] Jung D, Kim Y, Lee U, Lee H. Optimum design of the electric vehicle traction motor using the hairpin winding. In: Proc. IEEE 75th Veh. Technol. Conf.; 2012. p. 1–4.
[48] Jurkovic S, Rahman KM, Savagian PJ. Design, optimization and development of electric machine for traction application in GM battery electric vehicle. In: Proc. 2015 IEEE International Electric Machines & Drives Conference (IEMDC), Coeur d'Alene, ID; 2015. p. 1814–9.
[49] Rahman K, Jurkovic S, Hawkins S, Tarnowsky S, Savagian P. Propulsion system design of a battery electric vehicle. IEEE Electrification Magazine; 2014.
[50] Ehsani M, Gao Y, Longo S, Ebrahimi K. Modern electric, hybridelectric, and fuel cell vehicles: fundamentals, theory, and design. Englewood Cliffs, NJ, USA: CRC Press; 2018.
[51] Luna J, Costa-Castelló R. Chattering Free High Order Sliding Mode Observer for Estimation of Liquid Water Fraction in a Proton Exchange Membrane Fuel Cell. In: Proc. IEEE 2018 European Control Conference (ECC); 2018. p. 1226–31.
[52] Günther S, Ulbrich S, Hofmann W. Driving cycle-based design optimization of interior permanent magnet synchronous motor drives for electric vehicle application. In: Proc. International Symposium on Power Electronics, Electrical Drives; 2014. p. 25–30. Automation and Motion.
[53] Florian K, Doruk ÖE, Stephan S, Martin B, Bülent C, Bob M, Taeck LO, Horst F. Electrification of transport logistic vehicles: a techno-economic assessment of battery and fuel cell electric transporter. In: Proc. EVS28 International Electric Vehicle Symposium and Exhibition; 2015. p. 1–11.
[54] André M. The ARTEMIS European driving cycles for measuring car pollutant emissions. Sci Total Environ 2004;334:73–84.
[55] André M, Joumard R, Vidon R, Tassel P, Perret P. Real-world European driving cycles, for measuring pollutant emissions from high- and low-powered cars. Atmos Environ 2006;40(31):5944–53.
[56] Sileghem L, Bosteels D, May J, Favre C, Verhelst S. Analysis of vehicle emission measurements on the new WLTC, the NEDC and the CADC. Transp Res D, Transp Environ 2015;32:70–85.
[57] Hyundai Motors. KONA Electric. https://www.hyundai.com/in/en/find-a-car/kona-electric/specification. Accessed: 2021-06-15.
[58] BorgWarner. Drivetrain Systems. 2011, https://evwest.com/support/borgwarnere drive.pdf. Accessed: 2021-06-15.
[59] Klein MP, Park JW. Current Distribution Measurements in Parallel-Connected Lithium-Ion Cylindrical Cells under Non-Uniform Temperature Conditions. J Electrochem Soc 2017;164(9).
[60] H.E. Perez. Model Based Optimal Control, Estimation, and Validation of Lithium-Ion Batteries. Ph.D. dissertation, Dept. Civil and Environmental Eng.; California Univ.; Berkeley, CA, USA.
[61] Chinthavali M, Otaduy P, Ozpineci B. Comparison of Si and SiC inverters for IPM traction drive. In: Proc. IEEE Energy Convers. Congr. Expo.; 2010. p. 3360–5.
[62] BROMBACH J, SCHRÖTER T, LÜCKEN A, SCHULZ D. Optimizing the Weight of an Aircraft Power Supply System through + /- 270 VDC Main Voltage. Przegląd Elektrotechniczny 2012;1(47):47–50.
[63] Markel T, et al. ADVISOR: a systems analysis tool for advanced vehicle modeling. J Power Sources 2002;110(2):255–66.
[64] Lim M, Chai S, Yang J, Hong J. Design and Verification of 150-krpm PMSM Based on Experiment Results of Prototype. IEEE Trans Ind Electron 2015;62(12):7827–36.
[65] Lee B, Kwon S, Sun T, Hong J, Lee G, Hur J. Modeling of core loss resistance for D-q equivalent circuit analysis of IPMSM considering Harmonic Linkage Flux. IEEE Trans Magn 2011;47(5):1066–9.
[66] Hwang SW, Ryu JY, Chin JW, Park SH, Kim DK, Lim MS. Coupled electromagnetic-thermal analysis for predicting traction motor characteristics according to electric vehicle driving cycle. IEEE Trans Veh Technol 2021;70(5):4262–72.
[67] Preindl M, Bolognani S. Optimal state reference computation with constrained MTPA criterion for PM motor drives. IEEE Trans Power Electron 2015;30(8):4524–35.
[68] Sun T, Wang J, Chen X. Maximum torque per ampere (MTPA) control for interior permanent magnet synchronous machine drives based on virtual signal injection. IEEE Trans Power Electron 2015;30(9):5036–45.
[69] Storn R, Price K. Differential evolution-A simple and efficient heuristic for global optimization over continuous spaces. J Global Optim 1997;11(4):341–59.
[70] Pyrhönen J, Jokinen T, Hrabovcová V. Design of Rotating Electrical Machines. 2nd ed. John Wiley & Sons; 2013.
[71] Chin J, Cha K, Park J, Hong J, Lim M. Study on AC resistance of winding according to configuration of strands. In: Proc. 2019 IEEE Energy Conversion Congress and Exposition (ECCE); 2019. p. 3137–43.
[72] IEC60404-2: 'Magnetic materials – Part 2: methods of measurement of the magnetic properties of electrical steel sheet and strip by means of an Epstein frame'; 2008.
[73] Chen YS, Zhu ZQ, Howe D. Calculation of D- and q-axis inductances of PM brushless ac machines accounting for skew. IEEE Trans Magn 2005;41(10):3940–2.
[74] Chen H, Chen Y, Huang S, Zhang F. Calculation of inductance of permanent magnet synchronous motor considering permanent magnet flux linkage variation of load conditions. In: Proc. 2014 IEEE Conference and Expo Transportation Electrification Asia-Pacific (ITEC Asia-Pacific); 2014. p. 1–6.
[75] A. Palmgren, Ball and roller bearing engineering, 3rd ed. Burbank, Philadelphia, PA; 1959.
[76] Harris TA, Kotzalas MN. Advanced concepts of bearing technology-rolling bearing analysis. Boca Raton, FL: CRC Press.; 2007.
[77] Wrobel R, Mellor PH, Popescu M, Staton DA. Power loss analysis in thermal design of permanent-magnet machines—a review. IEEE Trans Ind Appl 2016;52(2):1359–68.

[78] Lee J, Lee J, Kim K. Design of a WFSM for an electric vehicle based on a nonlinear magnetic equivalent circuit. IEEE Trans Appl Supercond 2018;28(3):1–4.
[79] Salameh M, Spillman T, Krishnamurthy M, Brown IP, Ludois DC. Wound field synchronous machine with segmented rotor laminations and die compressed field winding. In: Proc. 2019 IEEE Energy Conversion Congress and Exposition (ECCE); 2019. p. 1739–46.
[80] J.H. Kim, D.M. Kim, Y.H. Jung and M.S. Lim. Design of ultra-high-speed motor for FCEV air compressor considering mechanical properties of rotor materials. IEEE Trans Energy ConversEarly Access.

Min-Ro Park received the bachelor's degree in electrical engineering from Chungnam National University, Daejeon, South Korea, in 2013 and the integrated master's and Ph.D. degrees in automotive engineering from Hanyang University, Seoul, South Korea, in 2020. Since 2020, he has been with Korea Institute of Robotics and Technology Convergence (KIRO), Pohang, South Korea, where he is currently a Senior Researcher. His research interests include multi-physics analysis and design of electric machine for mechatronics systems.

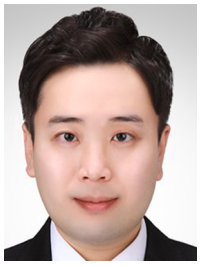

Dong-Min Kim received the B.S. degree in electronic system engineering, and the Ph.D. degree in automotive engineering from Hanyang University, Seoul, South Korea, in 2013 and 2021, respectively. In 2021, he was a Postdoctoral Researcher in Hanyang University, Seoul, South Korea. Since 2021, he has been with Honam University, Gwangju, South Korea, where he is currently an Assistant Professor. His research interests include design optimization of electric machines for automotive and industrial applications, modeling and optimization of electric vehicles, hybrid electric vehicles, and fuel cell electric vehicles.

Young-Hoon Jung received Bachelor's degree in mechanical engineering from Hanyang University, Seoul, South Korea, in 2013. Also, he received the integrated Master's and Ph.D. degree in automotive engineering from Hanyang University, Seoul, South Korea, in 2020. Since 2020, he has been with R&D Division of Hyundai Motor Company, Hwaseong, South Korea, where he is currently a Senior Research Engineer. His research interests are electric machine design for automotive and robot applications, and ultra-high speed motors.

Myung-Seop Lim received the Bachelor's degree in mechanical engineering from Hanyang University, Seoul, South Korea, in 2012. Also, he received the Master's and Ph.D. degree in automotive engineering from the same university, in 2014 and 2017, respectively. From 2017 to 2018, he was a Research Engineer in Hyundai Mobis, Yongin, South Korea. From 2018 to 2019, he was an Assistance Professor in Yeungnam University, Daegu, South Korea. Since 2019, he has been with Hanyang University, Seoul, South Korea, where he is currently an Assistant Professor. His research interests include electromagnetic field analysis and electric machinery for mechatronics systems such as applications.